scientific reports

Check for updates

OPEN

Hybrid sine cosine and spotted Hyena based chimp optimization for PI controller tuning in microgrids

Saleem Mohammad✉ & S. D. Sundarsingh Jeebaseelan

In this paper, a novel hybrid sine-cosine and spotted Hyena-based chimp optimization algorithm (hybrid SSC) is adopted for the precise tuning of proportional-integral (PI) controllers in a microgrid system. The microgrid integrates multiple renewable energy sources, including photovoltaic (PV) panels, wind turbines, a fuel cell, and a battery storage system, all connected to a common DC bus. This DC bus interfaces with the main grid through a voltage source converter (VSC). The microgrid comprises a total of eight PI controllers distributed across various components: the boost converter in the wind system, the fuel cell system, the battery energy storage device, and the VSC controller. The hybrid SSC optimization algorithm effectively combines the exploration capabilities of the sine-cosine algorithm (SCA) with the exploitation strengths of the spotted Hyena optimizer (SHO) and Chimp optimization algorithm (ChOA), aiming to achieve optimal tuning of the PI controllers. This hybrid approach ensures an enhanced dynamic response and overall system performance by minimizing the integral of the time-weighted squared error (ITSE) for each controller. The simulation results, directed in a MATLAB/SIMULINK environment, demonstrate the efficacy of the hybrid SSC algorithm in improving the stability, response time and efficacy of the microgrid. The proposed technique significantly outperforms traditional tuning techniques, ensuring robust operation and seamless addition of renewable energy sources with the main grid. This study contributes to the advancement of intelligent control strategies for modern microgrids, emphasizing the importance of hybrid optimization algorithms in achieving optimal performance in complex energy systems.

Keywords Hybrid optimization algorithm, Sine-Cosine Algorithm (SCA), Spotted Hyena Optimizer (SHO), Chimp optimization algorithm (ChOA), Proportional-integral (PI) controllers, Microgrid, Renewable energy integration, Integral of Time-Weighted Squared Error (ITSE)

Distributed generation (DG) provides a crucial solution to the numerous challenges encountered by energy systems globally. These include power stability, system reliability, network overloading, greenhouse gas emissions, and high consumption costs[1]. In the context of microgrids for commercial buildings, the implementation of an energy management system (EMS) has proven challenging in minimizing network load deviation and operational costs[2]. By integrating an EMS into Mult energy microgrids (MGs), there is significant potential to reduce the operational price and enhance the energy utilization efficacy[3]. DGs include a diverse array of energy resources, comprising renewable sources such as biomass, PV systems, and wind turbines (WTs), as well as nonrenewable options such as diesel generators (DiGs), gas engines (GE), and microturbines (MTs)[4].

Microgrids face numerous challenges stemming from fluctuations in demand, voltage, and frequency. Critical challenges in microgrid operation include managing reverse power flow, voltage stability, transient behaviors during islanded operations, significant frequency variations, and uncertainties in supply-demand dynamics. To ensure balanced load division, mainly under weak system conditions, microgrids often employ advanced control strategies[5]. Microgrids incorporating renewable energy sources such as PV panels, WTs, fuel cells, and battery storage systems require effective control strategies to manage the complex interactions between these components. PI control is used as a control strategy because of its simplicity and efficacy in maintaining system stability and performance[6].

Department of Electrical and Electronics Engineering, Sathyabama Institute of Science & Technology, Chennai 600119, India. ✉email: saleem238@gmail.com

Different types of control strategies have been implemented in the literature by researchers for efficient operation of microgrids. For voltage and frequency control in a microgrid, PI controllers are used to control the voltage and frequency at the local level. This involves adjusting the power output of distributed generation units (e.g., PV, wind) to match the load demand. This control strategy manages the power swap in the microgrid and the main grid. It optimizes the overall operation of the microgrid, balancing economic and technical objectives[7]. For efficient power sharing[8], droop control can be used, which implements decentralized control using droop characteristics to share active and reactive power in distributed generators without the need for communication. PI controllers help fine-tune the droop characteristics to achieve accurate power sharing. Load frequency control[9] maintains a balance between load demand and the power supply. PI controllers change the power output of generators to stabilize the system frequency under varying load conditions.

PI controllers are used in MPPT algorithms to optimize the power output from PV panels and WTs by adjusting the operating points to harvest maximum energy[1011]. In the case of battery energy management, PI controllers manage the charging and discharging cycles of the battery to hold the SOC within safe limits, ensuring the longevity and reliability of the battery system[12]. PI controllers regulate the battery's power output to smooth out load variations, reduce peak demand and maintain a stable power supply[13]. For grid synchronization, PI controllers ensure seamless synchronization of the microgrid by the main grid, managing the phase, frequency, and voltage alignment during grid-connected operations[14]. For island detection, PI controllers facilitate the transition in grid-connected and islanded modes, indicating the stability and continuity of the power supply during islanded operation.

In the case of reactive power and voltage control, PI controllers adjust the reactive power output of inverters and other compensating devices to regulate the voltage levels within the microgrid, enhancing power quality and reducing losses[15]. During voltage sags or swells, these controllers dynamically adjust the reactive power to stabilize the voltage, protecting sensitive equipment and ensuring reliable operation[16]. In fault detection and management, PI controllers enable distributed generators to ride through faults by adjusting their power output, ensuring continuous operation during short-term disturbances[17]. These controllers coordinate with protection devices to isolate faulty sections of the microgrid, minimizing the impact on the overall system.

Proper tuning of the PI controller is essential for achieving the desired execution in terms of stability, efficacy, and power quality. RESs such as PVs and wind are inherently variable due to changing weather conditions. A PI controller must be finely tuned to respond quickly and accurately to these variations to maintain system stability. Microgrids often travel with the main grid. Proper tuning ensures smooth transitions among grid-connected and islanded modes, maintaining stable operation during such transitions. Fluctuations in renewable energy generation can cause voltage instability. A PI controller helps maintain voltage levels within acceptable limits, thus ensuring a stable power supply to the loads.

The Ziegler–Nichols method is a heuristic tuning method that provides initial tuning factors that are related to the system's response[18]. The Cohen–Cooper method is another heuristic tuning method that is suitable for processes with significant delays[19]. Modern control systems often utilize software tools for tuning PI controllers. These tools use advanced algorithms and simulations to optimize controller parameters. Advanced optimization techniques, such as genetic algorithms, are applied to find optimal PI controller settings by exploring a wide range of possible parameters[20]. Optimization algorithms for tuning PI controllers provide a systematic and often automated approach to determining the optimal controller parameters that achieve the desired performance metrics. These algorithms are particularly useful for complex or nonlinear systems where traditional tuning methods may not yield satisfactory results. These algorithms provide powerful tools for tuning PI controllers in complex and dynamic systems. By systematically searching for optimal parameters, these algorithms improve the execution, stability, and robustness of the control system. The choice of algorithm depends on certain characteristics of the system, the type of optimization problem, and the desired performance criteria[21].

In recent research, innovative methodologies inspired by natural phenomena have emerged to address complex challenges across various domains. The key among these methodologies are the genetic algorithm (GA)[22], particle swarm optimization (PSO)[23], and other advanced techniques[24]. The Dandelion Optimizer Algorithm (DOA)[25] is inspired by the dandelion's dispersal strategy, focusing on balancing exploration and exploitation during optimization. While DOA effectively escapes local minima, its random dispersal patterns sometimes lack fine-tuning capabilities in the exploitation phase. The Coati Optimization Algorithm (COA)[26] is inspired by the social behavior of coatis and demonstrates strong performance in exploration through swarm intelligence. However, COA can struggle with convergence speed, especially in handling high-dimensional problems. Crayfish Optimization Algorithm (CFOA)[27] is based on the behavioral patterns of crayfish, especially their random movement strategies. While it excels in exploration, it often lacks focused exploitation, resulting in slower convergence in certain cases. The Binary Waterwheel Plant Optimization (BWPO) algorithm[28], inspired by waterwheel systems, is effective for binary optimization problems. However, its utility in continuous optimization is limited by its discrete nature. Harris Hawk Optimization (HHO)[29] is an established metaheuristic algorithm known for its fast convergence and strong performance in both exploration and exploitation. However, its global search can sometimes be less diverse, leading to suboptimal solutions in highly complex landscapes.

Researchers have also introduced updated versions of these methods to increase their efficacy. In a recent study by[30], a new approach called the chaos cultural sine–cosine algorithm (CCSCA) was proposed to address the issue of premature convergence encountered in the sine–cosine algorithm (SCA). This novel method features a cultural algorithm for population structuring and integrates chaotic techniques for optimizing the search process. Performance evaluations conducted on standard functions revealed that CCSCA outperforms the basic SCA algorithm in terms of global search capability, consistently delivering superior results. Building upon this progress[31], proposed a binary version of the sine–cosine algorithm (SCA) tailored specifically for solving profit-based unit commitment (PBUC) problems. This binary SCA method uses modified sigmoid functions to map the continuous search space. Comparative studies demonstrated the efficacy of the binary

SCA approach, highlighting its competitive edge over alternative methods in addressing PBUC challenges. Furthermore[32], introduced a discrete variant of the sine–cosine algorithm (SCA) designed to address intricate discrete optimization problems. The efficacy of this discrete SCA was validated by extensive benchmarking against various functions, highlighting its efficiency and superiority over existing approaches in similar problem domains. These advancements underscore the versatility and robustness of the sine–cosine algorithm (SCA) family, demonstrating its adaptability to different problem types through innovative adaptations and enhancements. These methodologies not only expand the toolkit of optimization techniques but also pave the way for more effective solutions in diverse application areas.

Recent studies have introduced several innovative hybrid algorithms based on the SCA, each tailored to enhance optimization capabilities across various domains. In[33], researchers developed a hybrid algorithm that integrates principles and operators from different algorithms, enhancing both exploration and exploitation abilities. By combining these features, the hybrid SCA method effectively addresses optimization problems. The study evaluated the algorithm's performance via seven benchmark functions, demonstrating its superior efficiency compared with other existing approaches. This hybrid approach proved to be highly competitive in delivering optimal solutions. Similarly[34], proposed the steady-state genetic algorithm (SSGA), a hybrid method designed specifically for engineering design problems. The SSGA combines the search capabilities of the SCA with the ability of the steady-state genetic algorithm to prevent premature convergence. Through rigorous testing on complex engineering design problems, the SSGA approach significantly improved performance outcomes, highlighting its superiority over alternative optimization methods. In[35], an updated approach utilizing the SCA was introduced, integrating advanced strategies such as opposition learning and opposition-based learning methods. These enhancements aim to increase the efficacy and convergence rate of global search in solving diverse optimization problems. An evaluation across 23 benchmark functions confirmed that the updated SCA method outperformed other approaches by a significant margin, highlighting its effectiveness in achieving high-quality solutions. Furthermore[36], developed the hybrid sine–cosine algorithm (HSCA), which leverages the SCA's capabilities to address various optimization challenges. HSCA consistently outperforms alternative methods, particularly in scheduling tasks across multiple scenarios. Its ability to generate superior outcomes underscores its effectiveness in addressing complex optimization problems effectively.

In recent research, a novel hybrid algorithm named the Mult objective sine-sine and sine-cosine algorithm (MOSSASCA) has been proven to address the challenge of determining the virtual positions of machines effectively. MOSSASCA integrates elements from both the SSA (Sine-Sine Algorithm) and the SCA (Sine-Cosine Algorithm) methodologies, aiming to optimize machine positioning while simultaneously addressing multiple objectives[37]. The primary goals of MOSSASCA include mitigating service quality violations, minimizing power consumption, prolonging the total agent termination time, and resolving conflicts among these objectives. This Mult objective approach seeks to find a solution that balances these conflicting goals in machine positioning optimization scenarios. To increase the efficiency of the SSA, a local search technique is embedded within the SCA framework. This integration serves to prevent the algorithm from converging prematurely to local optima and accelerates its convergence toward optimal solutions. By combining these strategies, MOSSASCA aims to achieve robust and efficient optimization results across a variety of scenarios. To evaluate the performance of MOSSASCA, extensive demonstrations involving both physical and digital devices were conducted. These evaluations compared the algorithm's outcomes against those of well-established Mult objective optimization (MOP) methods. The results demonstrate MOSSASCA's ability to balance the three primary objectives effectively: service quality, power consumption, and termination time. This balanced achievement underscores the algorithm's effectiveness in generating solutions that meet multifaceted optimization criteria in machine positioning tasks.

In recent studies, two innovative optimization algorithms have been introduced, each offering unique approaches to enhance efficiency and performance across different domains. In[38], researchers offered a novel linear weight loss method aimed at improving the convergence speed and optimizing the precision of optimization algorithms. This method focuses on aligning the global search capability with an exponential decay conversion parameter while also enhancing the local growth capacity. By integrating these features, the algorithm effectively prevents convergence into local optima, thereby achieving faster convergence and superior optimization results. Simulation experiments validated the efficacy of this approach, demonstrating its ability to significantly increase the precision of the optimization processes. In[39], the hybrid particle swarm and spotted Hyena optimizer (HPSSHO), a hybrid metaheuristic algorithm designed to address complex optimization problems, was presented. This innovative approach combines the strengths of Particle Swarm Optimization (PSO) and the Spotted Hyena Optimization (SHO) algorithm. The HPSSHO algorithm was rigorously evaluated against four other prominent metaheuristic algorithms through extensive experiments. The results showcased its superior performance across various benchmarks, highlighting its efficiency in achieving optimal solutions compared with its counterparts.

In[40], researchers introduced a novel approach known as the lateral inhibition-based spotted hyena optimizer (LI-SHO), which is designed specifically to address complex image pairing problems. This innovative method integrates the lateral inhibition mechanism into the Spotted Hyena Optimizer (SHO), enhancing the preprocessing phase of image data to improve intensity gradients and contrast. These enhancements aim to refine the characteristics of the images, thereby increasing the accuracy and efficiency of the subsequent image matching processes. The LI-SHO approach leverages the lateral inhibition mechanism, a biologically inspired concept where neurons inhibit the activity of neighboring neurons, enhancing the contrast and sharpening edges in image data. By integrating this mechanism into SHO, the algorithm effectively preprocesses images, optimizing them for better feature extraction and matching. Experimental evaluations conducted to assess the performance of LI-SHO over other competitive algorithms demonstrated its superior effectiveness and feasibility

in handling image matching tasks. The results underscore the ability of LI-SHO to produce more accurate and reliable results than traditional and other state-of-the-art algorithms in the field.

In[41], a novel approach combining the Spotted Hyena Optimizer (SHO) and ant lion optimization (ALO) methods was developed to determine the soil shear strength, addressing the limitations of traditional artificial neural network (ANN) models in this context. This study aimed to increase the accuracy and reliability of soil shear strength predictions by integrating these metaheuristic algorithms with ANNs. Initially, two hybrid models were created: ALO-ANN and SHO-ANN. These models were structured and refined through an orderly trial-and-error process to determine the optimal configurations that could effectively predict the shear strength of the soil. This iterative approach involves adjusting the parameters and architectures of the ANN while leveraging the optimization capabilities of ALO and SHO to improve model performance. The experimental results revealed the effectiveness of both ALO and SHO in enhancing the predictive accuracy of the ANN models. Specifically, the ALO-ANN model achieved a significant reduction in prediction error, approximately 35%, highlighting its robust ability to refine predictions on the basis of soil data. Moreover, the SHO-ANN model also demonstrated substantial improvement, with an error reduction of approximately 18%, emphasizing its effectiveness in optimizing the ANN's predictive capabilities.

In[42], researchers introduced a new method based on SHO. This approach was developed to address the challenges associated with selecting optimal features in complex datasets, aiming to enhance execution in spatial search and feature selection tasks. The suggested method leverages the unique capabilities of SHO, a metaheuristic algorithm taught by the foraging behavior of spotted hyenas. SHO is particularly adept at balancing exploration and exploitation to search efficiently through solution spaces and optimize outcomes. To evaluate the efficacy of their method, the researchers conducted trials comparing the SHO-based feature selection method against other existing techniques. The experimental results showed that the proposed algorithm consistently exceeded the alternatives in both accuracy and efficiency. Specifically, the SHO-based feature selection method exhibited superior performance in spatial search tasks, effectively identifying relevant features that contribute most significantly to the predictive power of the models. This capability is crucial in data-driven applications where selecting the right subset of features can increase model performance, ease computational complexity, and improve interpretability.

In recent years, a variety of optimization algorithms inspired by natural processes have gained prominence as effective tools for solving intricate optimization problems. These algorithms draw insights from the behaviors observed in nature and leverage their inherent intelligence to seek optimal solutions. One notable algorithm in this domain is the hybrid sine-cosine and spotted Hyena-based chimp optimization algorithm (hybrid SSC). The hybrid SSC algorithm integrates features from both the SCA and the Spotted Hyena Optimizer (SHO), combining their respective strengths to balance exploration and exploitation approaches throughout the optimization process. The SCA is renowned for its ability to balance global and local searches via sine and cosine functions, which aids in efficient exploration of the solution space. Instead, the Spotted Hyena Optimizer mimics the hunting behavior of hyenas to optimize objective functions through intelligent search strategies. By merging these two methods, the hybrid SSC algorithm aims to capitalize on their complementary attributes. It leverages the exploration capabilities of the SCA with adaptive and dynamic search mechanisms inspired by hyena behavior from SHO. This combination enhances the algorithm's robustness in carrying out complex optimization tasks by effectively navigating diverse solution landscapes and improving convergence toward optimal solutions. The hybrid SSC algorithm signifies significant progress in optimization techniques, offering a versatile and efficient approach to solving real-world optimization challenges in various domains. Its ability to integrate multiple strategies derived from natural behaviors underscores its potential as a powerful tool for researchers and practitioners seeking innovative solutions to complex optimization problems.

The hybrid SSC stands out because of its numerous advantages, which include enhanced convergence speed, robustness, and ability to tackle Mult objective optimization challenges effectively. This algorithm merges elements from the SCA and the SHO, harnessing their respective strengths to achieve balanced exploration and exploitation in the optimization method. One of the key applications of the hybrid SSC algorithm is in power flow control strategies. By integrating this innovative algorithm, it becomes possible to optimize the allocation of power generation from diverse distributed generation (DG) sources. This optimization aims to mitigate grid congestion, enhance voltage stability, and minimize system losses within the power grid infrastructure. The algorithm's enhanced convergence speed enables it to quickly converge toward optimal solutions, which is crucial in dynamic and real-time operational environments. Its robustness ensures reliable performance across varying conditions and complexities inherent in power systems. Moreover, the hybrid SSC algorithm's ability to handle Mult objective optimization problems allows it to simultaneously optimize conflicting objectives such as minimizing system losses while maximizing renewable energy utilization. Implementing the hybrid SSC algorithm in power flow control strategies enhances the efficacy of renewable energy utilization and the sustainability and reliability of the power grid. By optimizing power generation allocation, the algorithm helps reduce dependency on fossil fuels, mitigate environmental impacts, and support the transition toward cleaner energy sources.

The motivation for this study stems from the increasing complexity of modern microgrids, which integrate multiple renewable energy sources such as PV, wind, fuel cells, and battery storage systems. These distributed energy resources, while promoting sustainability and energy independence, present significant challenges in terms of system control and stability, particularly when interfacing with the main grid. Precise tuning of Proportional-Integral (PI) controllers is essential for ensuring optimal performance, stability, and dynamic response in such complex systems. However, conventional tuning methods often fall short in handling the nonlinearities and variability inherent in microgrids.

To address these challenges, the development of advanced optimization algorithms becomes crucial. This paper introduces a novel hybrid optimization approach that leverages the strengths of multiple algorithms—

Sine-Cosine, Spotted Hyena, and Chimp optimizers. By combining the exploration and exploitation capabilities of these algorithms, the hybrid SSC method aims to achieve more precise tuning of PI controllers, improving system response, stability, and efficiency. The motivation behind this research is to enhance the reliability and performance of microgrids, enabling seamless integration of renewable energy sources while minimizing errors and operational disturbances. This work contributes to the advancement of intelligent control techniques in the growing field of microgrid technology.

The specific objectives of this study include the following:

- A mathematical model that captures the characteristics and constraints of grid-integrated hybrid DG systems is developed.
- The hybrid SSC algorithm is implemented and integrated into the power flow control strategy.
- Extensive simulations and performance evaluations are conducted to assess the effectiveness and efficacy of the suggested algorithm.
- The results are compared with those of existing optimization techniques to demonstrate the control of the hybrid SSC algorithm.
- Analyzing the impact of optimized power flow control on system performance metrics such as power loss and voltage stability,

Control methods of hybrid DG systems

The control of the hybrid distributed generation system (HDGS) is accurately shown by incorporating the hybrid SSC optimization algorithm, as shown in Fig. 1. The HDGS integrates various RESs, including a WT, PV system, fuel cell, and battery storage system, all working together to facilitate seamless energy transfer in the DC bus. Dynamic optimization techniques are applied to determine the PI controller gains, ensuring efficient power management and maximizing the electrical energy output of the system. The power flow management and control modules in the HDGS unit are designed in the operational modes of both the load and the grid. In grid-connected operations, the HDGS unit's active and reactive output powers are dynamically adjusted to match their reference values. To do this, the VSI-based control system selects the right power control mode to confirm the execution and system stability.

To handle altering load demands, adjusting the power contributions by both the main grid and the HDGS flexibly is essential. This requires providing a steady supply of active and reactive power by effectively controlling the power flow in the HDGS and the utility grid. Additionally, maintaining a reliable connection between the main grid power and the HDGS is necessary to obtain the overall load demand. The power balance equation is satisfied by both the DC link and the PCC, as shown in the equation[43].

$$P_{HDGS}(t) = P_{windturbine}(t) + P_{photovoltaic}(t) + P_{FuelCell}(t) + P_{battery}(t) \tag{1}$$

The power flow balance in the system is calculated via Eq. (1), which includes the total power flow model. This is determined by factoring in the output of the HDGS and the load demand. Equations 2 and 3 are utilized to calculate $P_{GRID}(t)$ and $P_{LOAD}(t)$, respectively, whereas Eqs. 4 and 5 are employed to determine $Q_{LOAD}(t)$ and $Q_{GRID}(t)$[43].

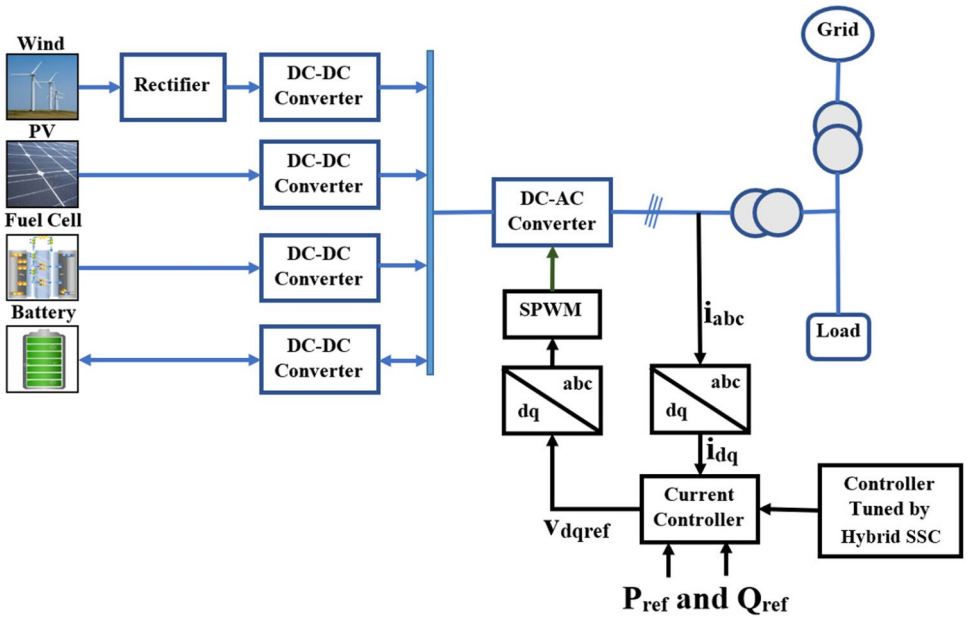

Figure 1. Management structure of HDGS with the proposed controller.

$$P_{GRID}(t) = [P_{LOAD}(t) - P_{HRES}(t)] \tag{2}$$

$$P_{LOAD}(t) = [P_{HRES}(t) + P_{GRID}(t)] \tag{3}$$

$$Q_{GRID}(t) = [Q_{LOAD}(t) - Q_{HRES}(t)] \tag{4}$$

$$Q_{LOAD}(t) = [Q_{HRES}(t) + Q_{GRID}(t)] \tag{5}$$

The battery power of the storing unit is affected by how long it discharges, when it serves as an energy source, and how long it charges, when it acts as a load. However, maintaining a steady power balance is difficult because of the nonlinear changes in load demand and the unstable nature of renewable energy[44]. To address this issue, the HDGS unit needs to operate in high-performance mode for effective power control. The active and reactive power measurements are given by Eqs. (6) and (7).

$$P_I(t) = \tfrac{3}{2}[v_d * i_d + v_q * i_q] \tag{6}$$

$$Q_I(t) = \tfrac{3}{2}[v_q * i_d + v_d * i_q] \tag{7}$$

Wind generation by a PMSG with a DC–DC converter

The WT with a cross-sectional area of A provides access to available wind power[45].

$$P_{wind} = \tfrac{1}{2}\rho\, AV_w^3 \tag{8}$$

The density of air is denoted by ρ and measured in kg/m^3, whereas the wind speed is denoted by V_w and measured in m/s. The power coefficient C_p indicates the amount of power that can be extracted from the wind turbine for conversion[45].

$$P_w = C_p P_{wind} \tag{9}$$

The maximum value of C_p is the Betz limit of 0.593.

P_w is the power extracted by the rotor of the wind turbine and is given as[45]

$$P_w = \tfrac{1}{2}\rho\, AV_w^3 C_p(\beta, \lambda) \tag{10}$$

where λ is the tip speed ratio:

$$\lambda = \tfrac{w_r R}{V_w} \tag{11}$$

where R is the radius of the rotor in m, w_r is the rotor speed in rad/s, and β is the pitch angle.

In Fig. 2, a permanent magnet synchronous generator is combined with the DC microgrid via a diode bridge rectifier and a DC-to-DC boost converter[18].

$$d_{wind} = K_{p1}(I_{wref}(t) - I_w(t)) + K_{i1}\int (I_{wref}(t) - I_w(t))\, dt \tag{12}$$

The maximum power point tracking regulates the reference inductor current I_{wref} created from the rectifier to attain maximum power from the WT system at a specific DC bus voltage V_{dc}[45].

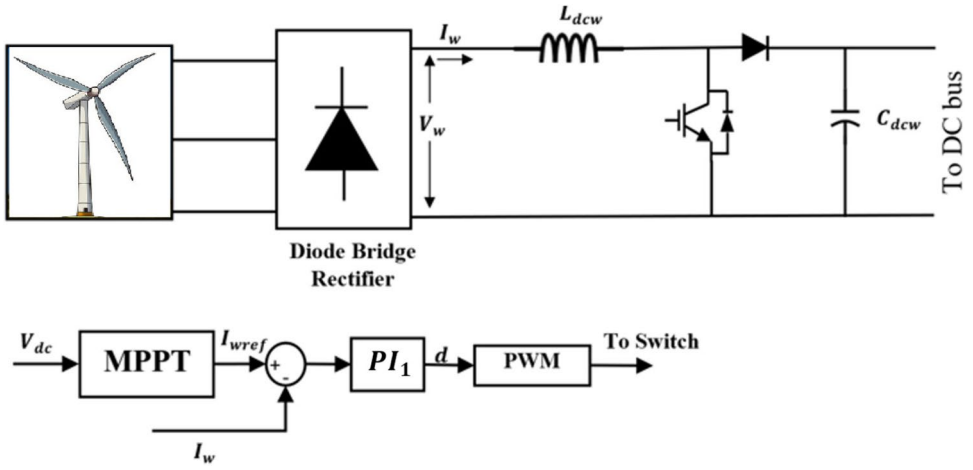

Figure 2. PMSG-based wind generation with a DC–DC converter.

The PI controller in the DC-DC converter control system adjusts the duty cycle of the switching pulses sent to the IGBT switch. This regulation ensures the maintenance of the desired current I_{wref} through the inductor. The current I_{wref} is shown by the MPPT algorithm for a specific V_{dc}. Maximum power extraction from the wind turbine occurs when the derivative of the power with respect to the rotor speed dP_w/dW_r is equal to zero. Since the back EMF (electromotive force) is directly proportional to the rotor speed, this relationship is established[46].

$$\frac{dP_w}{dV_{dc}} = 0 \tag{13}$$

The MPPT algorithm is employed to calculate the optimal value of the source inductor current, I_{wref}, corresponding to a specific DC bus voltage, V_{dc}. This enables the concept of maximum power from the PMSG. The adjustment of I_w is performed on the fluctuations in the DC link voltage observed at a given wind speed.

PV generation with an MPPT-based DC–DC converter

The basic circuit illustration of a solar panel is shown in Fig. 3.

The PV cell can be considered an ideal current source called I_{ph}, with series and parallel resistances, as shown in Fig. 3. The output current of an ideal solar cell is expressed as

$$I = I_{ph} - I_d \tag{14}$$

where I is the PV output current, I_d is the diode current, and I_{ph} is the photon current.

In semiconductor theory, the equation that describes the I-V characteristics of a PV cell is Shockley's diode current equation, shown as[47]

$$I_d = I_s \left[exp \left(\frac{qV_{oc}}{N_s KAT_o} \right) - 1 \right] \tag{15}$$

then

$$I_d = I_{ph} - I_s \left[exp \left(\frac{qV_{oc}}{N_s KAT_o} \right) - 1 \right] \tag{16}$$

where I_s represents the saturation current, q represents the electron charge, V_{oc} represents the open-circuit voltage, N_s represents the series of connected cells per module, K represents Boltzmann's constant, and T_o represents the nominal cell temperature in kelvin.

The efficient operation of PV systems relies heavily on maintaining optimal conditions to maximize power extraction from solar panels. Given the comparison of PV output to varying weather situations such as irradiance and temperature, the utilization of a DC-DC converter is indispensable. This module plays a role in setting both the output voltage and power of the PV arrays, ensuring that they operate at their peak efficiency. The MPP of a PV panel is where it operates most efficiently in terms of power output. This point, denoted as V_{mpp}, is vital for extracting maximum power from the PV arrays. The PV panel's power-voltage curve (P-V curve) illustrates this association, showing the peak power output at V_{mpp}. Figure 4 shows how controlling the PV voltage to align with V_{mpp} optimizes power extraction. The DC-DC converter alters the voltage to ensure that the PV panel operates at or near this optimal point, thereby maximizing energy production.

The P-V curve depicts the correlation between the power output (P) and the voltage (V) around the terminals of the PV panel. It is taken from the current-voltage curve (IV curve) and serves as a visual tool to identify the

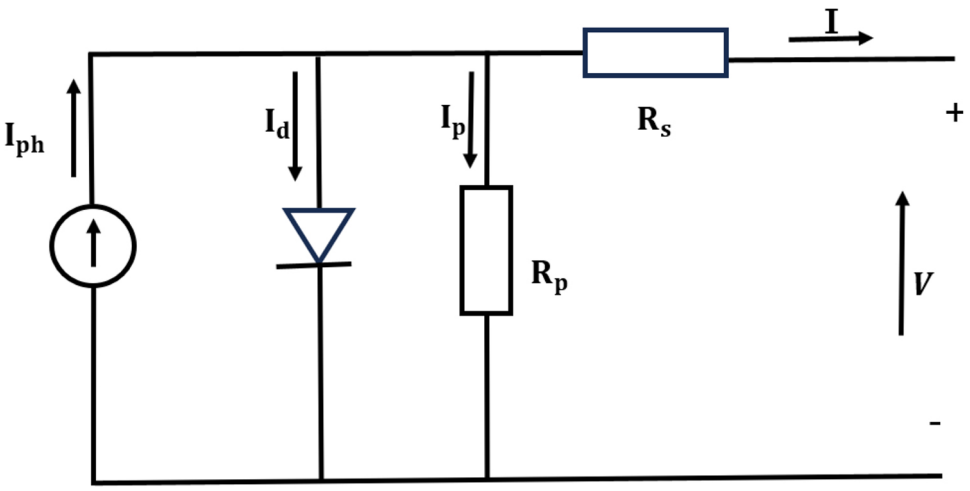

Figure 3. Equivalent circuit of the real model for the PV panel.

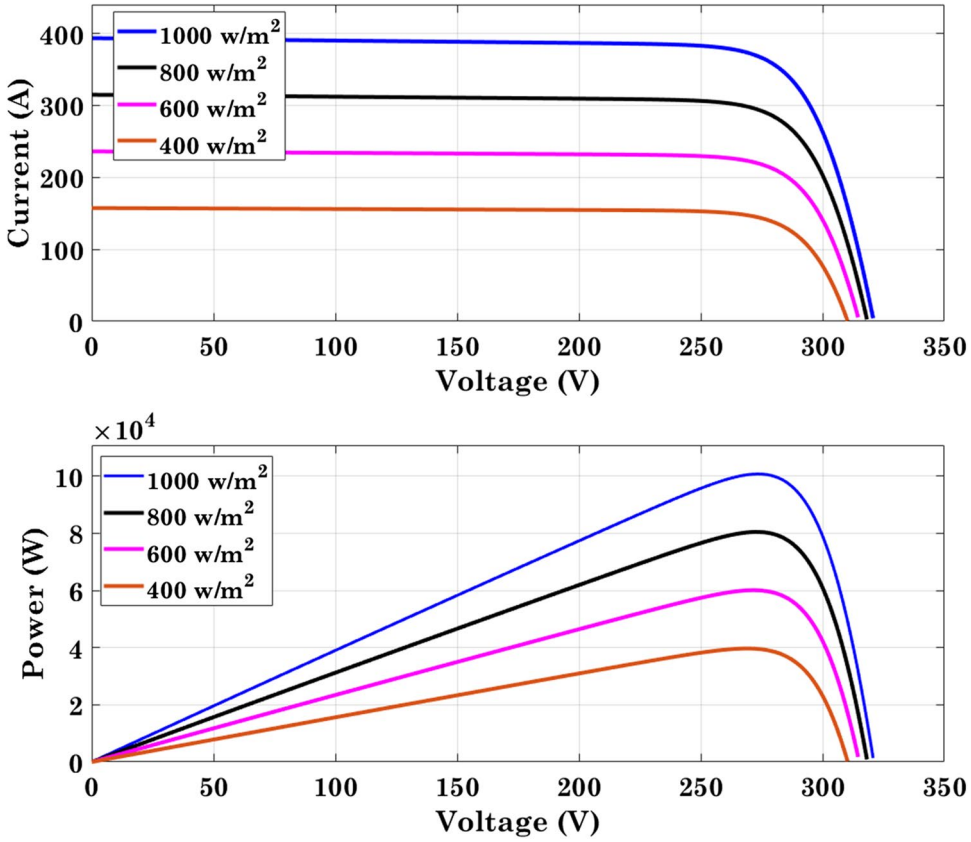

Figure 4. PV characteristics.

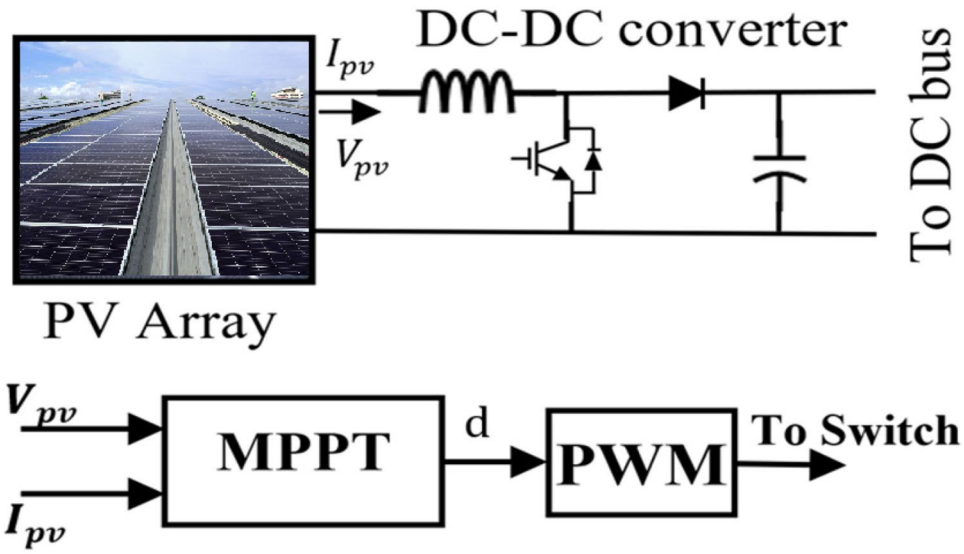

Figure 5. PV with an MPPT-operated DC–DC converter.

MPP. By monitoring and altering the operating voltage of the PV panel via the DC–DC converter, operators can ensure that the system operates efficiently regardless of fluctuations in solar irradiance or temperature. Figure 5 shows the DC–DC converter employed in PV systems, which converts the DC voltage from the PV array to a different DC voltage level fit for the load or storage system.

The converter's duty cycle is controlled by the MPPT algorithm to adjust the voltage and ensure that the PV panel works at V_{mpp}, maximizing energy efficiency and output. Efficient use of the DC–DC converter is critical

for system performance. It minimizes energy losses during conversion and ensures that the most available power from the PV arrays is utilized effectively.

The incremental conductance (INC) is used in the MPPT algorithm for PV systems. It continuously adjusts the PV panel's operating point to obtain the greatest power output. This algorithm is particularly effective in environments where solar irradiance levels fluctuate, as it dynamically responds to changes in the PV panel's voltage and current characteristics. The incremental conductance algorithm operates based on the principle of comparing the instantaneous conductance (slope of the P-V curve) of the PV panel with a reference conductance. Further details about the INC-based MPPT algorithm are extensively available in the literature[48], providing deeper insights into its operational principles and advantages in optimizing PV system performance.

Fuel cell system with a DC–DC converter

A fuel cell is an electrochemical device that changes chemical energy into electrical energy. It operates by combining hydrogen with oxygen in the air to generate electricity, heat, and water as byproducts. The fuel processor converts the fuel source (hydrogen, natural gas, methanol, etc.) into a form usable by the fuel cell stack. In the fuel cell stack, the electrochemical reaction occurs to produce electricity. A DC-DC converter is applied to step up or step down the voltage level of the electricity bent by the fuel cell stack to match the voltage requirements of the microgrid or other loads connected to the system. It plays a key role in managing the power flow by the fuel cell system and the microgrid. It typically converts the low-voltage DC output of the fuel cell stack (which can vary depending on the fuel cell technology and configuration) to a higher DC voltage suitable for the microgrid or for charging batteries/storage systems. The DC-DC converter is controlled to ensure efficient operation and to match the power output properties of the fuel cell system with the variable power demands of the microgrid or connected loads. Fuel cells can provide continuous power independently of weather conditions (unlike solar or wind power), enhancing the reliability of the microgrid. DC-DC converters enhance the efficacy of the system by optimizing the power transfer between the fuel cell and the microgrid. Microgrids with fuel cells and converters can maintain grid support services such as voltage and frequency control, contributing to grid stability.

Figure 6 shows a detailed schematic of a fuel cell system integrated with a DC-DC converter with its associated control strategy. This system aims to set the output voltage to meet the requirements of a microgrid or other connected loads. The control strategy affects the use of a PI controller to set the output voltage of the DC-DC converter. The PI controller processes the error in the output voltage and the required voltage to obtain the appropriate duty cycle for the DC-DC converter. The output of the PI controller is the duty cycle needed by the DC-DC converter. The duty cycle controls the switching of the converter, thereby regulating the output voltage. The duty cycle of the converter is[18]

$$d_{fuel} = K_{p2}\left(V_{dcref}\left(t\right) - V_{dc}\left(t\right)\right) + K_{i2}\int\left(V_{dcref}\left(t\right) - V_{dc}\left(t\right)\right)dt \tag{17}$$

Battery energy storage system with a DC–DC converter

The behavior of a battery in an electrical system is characterized by its SoC, which represents the ratio of its entire energy capacity that is currently available. This SoC is crucial for managing the battery's energy levels effectively over time.

The SoC of the battery at any given time t is defined as[49]:

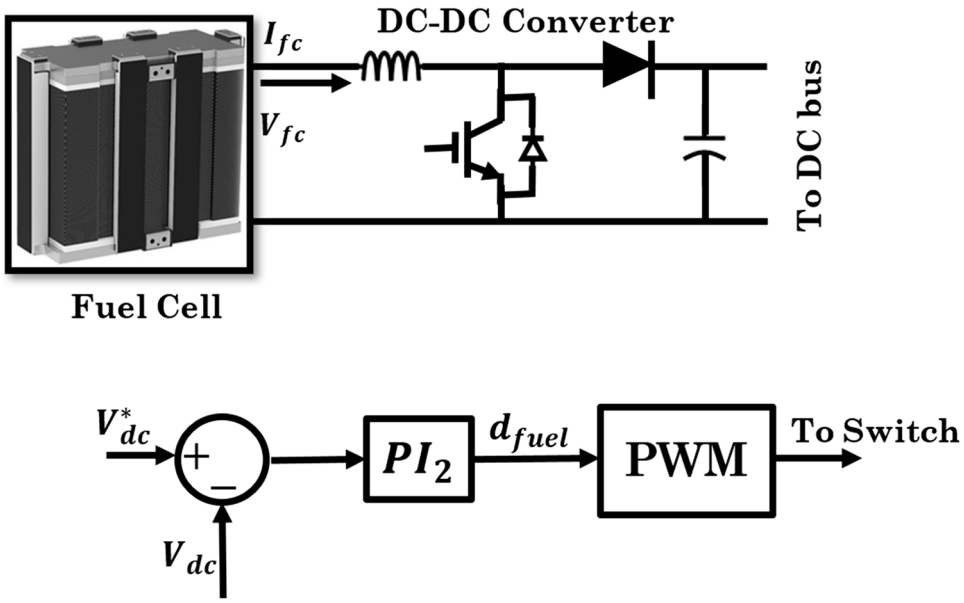

Figure 6. FC system with a DC-DC converter.

$$SoC\,(t) = \frac{BL\,(t)}{BL_{cap}} \times\ 100\% \tag{18}$$

where $BL\,(t)$ represents the battery's current energy level at time t. BL_{cap} denotes the initial nominal capacity of the battery. This equation indicates that the SoC is calculated by dividing the current energy level of the battery $BL\,(t)$ by its total capacity BL_{cap} and then multiplying by 100 to express it as a percentage.

The SoC is subject to upper and lower bounds to optimize the battery lifespan and performance:

$$SoC_{min} < SoC\,(t) < SoC_{max} \tag{19}$$

where SoC_{min} is the minimum allowable SOC and SoC_{max} represents the maximum allowable SOC. These constraints ensure that the battery operates within safe limits, avoiding overcharging or deep discharging, which can significantly impact battery health and longevity.

Figure 7 shows the combination of a battery into an electrical system by a DC-DC converter and a VSI to connect the battery to an AC bus. In the system described, PI controllers are used to set the operation of a bidirectional DC–DC converter allied to a battery. These controllers ensure that the battery voltage and current are maintained at the desired levels to optimize performance and efficiency. The first PI controller generates the reference battery current I^*_{bat} to compensate for the error in the DC converter output voltage V^*_{dc}(t) and the actual converter output voltage $V_{dc}\,(t)$. The equation governing this relationship is as follows[18]:

$$I^*_{bat} = Kp_3 \cdot\ (V^*_{dc}\,(t) - V_{dc}\,(t)) + Ki_3 \cdot \int\ (V^*_{dc}\,(t) - V_{dc}\,(t))\,dt \tag{20}$$

where Kp_3 and Ki_3 are the proportional and integral gains of the PI controller, respectively. $V^*_{dc}\,(t)$ is the desired DC converter output voltage. $V_{dc}\,(t)$ is the actual converter output voltage measured in the system.

The second PI controller causes the duty cycle d_{bat} based on the error in the battery current I_{bat} and reference battery current I^*_{bat}. The equation governing this relationship is as follows[18]:

$$d_{bat} = Kp_4 \cdot (I^*_{bat}\,(t) - I_{bat}\,(t)) + Ki_4 \cdot \int\ (I^*_{bat}\,(t) - I_{bat}\,(t))\,dt \tag{21}$$

Current control strategy of the DC–AC converter

In a hybrid distributed generation system (HDGS), precise control of active and reactive power delivery to the grid is needed to ensure stable, efficient operation. The control strategy presented in Fig. 8 involves several PI controllers to manage the power flow and maintain grid stability.

1. Reference Current Generation:

$$i^*_d = Kp_5 \cdot\ \left(P^*\,(t) - P\,(t)\right) + Ki_5 \cdot \int\ \left(P^*\,(t) - P\,(t)\right)\,dt \tag{22}$$

Kp_5 and Ki_5 are the proportional and integral gains, respectively, of the PI controller for active power control. $P^*\,(t)$ Reference active power setpoint. $P\,(t)$ Actual active power was delivered to the grid.

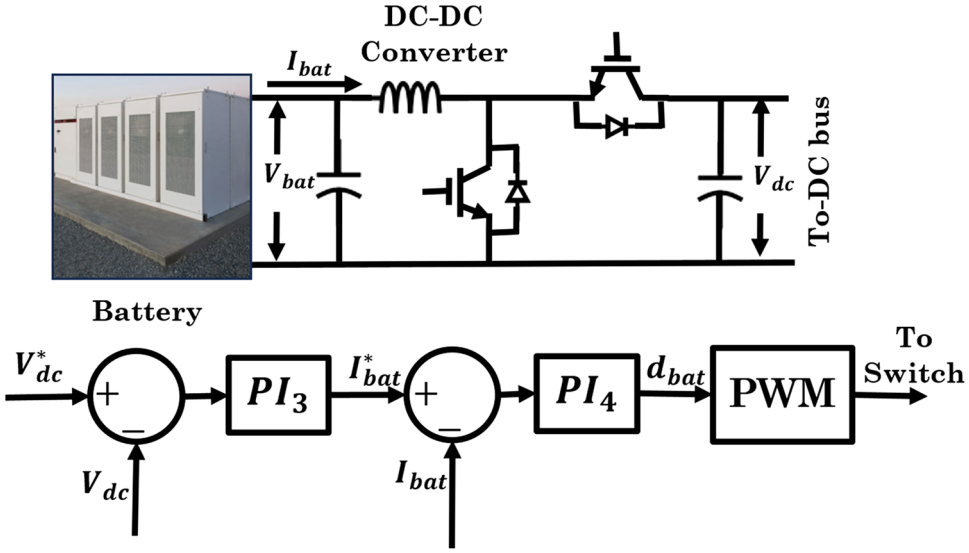

Figure 7. Battery storage system with a DC–DC converter.

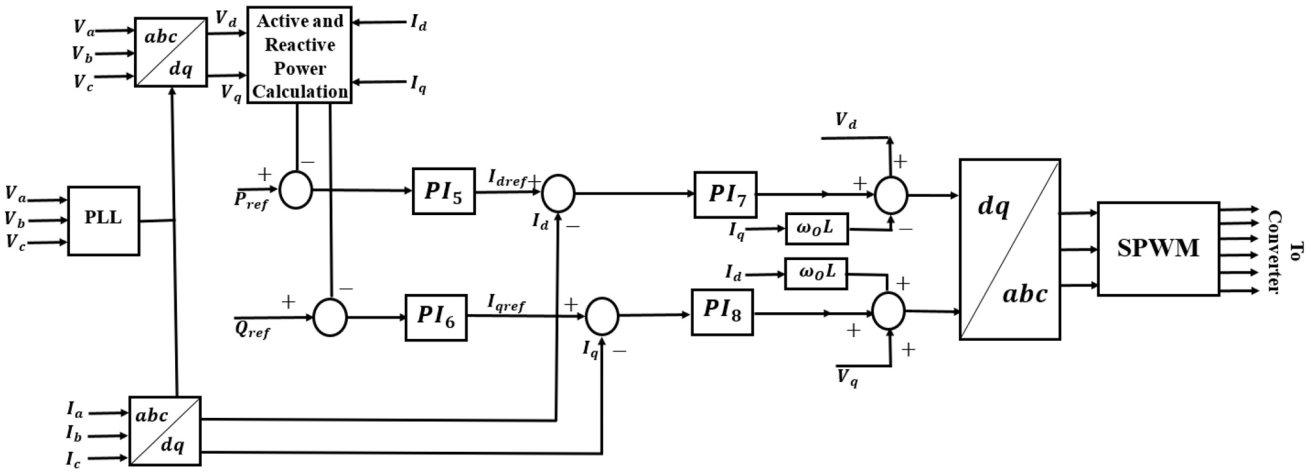

Figure 8. Control strategy of the DC–AC converter.

$$i_q^* = Kp_6 \cdot \left(Q^*(t) - Q(t)\right) + Ki_6 \cdot \int \left(Q^*(t) - Q(t)\right) dt \tag{23}$$

Kp_6 and Ki_6 proportional and integral gains of the PI controller for reactive power control. $Q^*(t)$ is the reference reactive power setpoint. $Q(t)$ is the actual reactive power sent to the grid.

These equations compute the reference current vectors i_d^* and i_q^* based on the error in the desired power and the actual power from the system. The proportional term offers an immediate response to current errors, but the integral term passes steady-state errors over time. These reference currents are used as inputs to control the inverter to adjust the generated voltage vectors, thereby managing the active and reactive power flows to the grid.

2. Voltage Vector Generation

$$V_d^* = Kp_7 \cdot \left(i_d^*(t) - i_d(t)\right) + Ki_7 \cdot \int \left(i_d^*(t) - i_d(t)\right) dt \tag{24}$$

Kp_7 and Ki_7 are the proportional and integral gains, respectively, of the PI controller for direct-axis current control.

$$V_q^* = Kp_8 \cdot \left(i_q^*(t) - i_q(t)\right) + Ki_8 \cdot \int \left(i_q^*(t) - i_q(t)\right) dt \tag{25}$$

Kp_8 and Ki_8 are the proportional and integral gains, respectively, of the PI controller for direct-axis current control.

These equations calculate the reference voltage vectors V_d^* and V_q^* based on the error in the source and actual currents in the direct and quadrature axes. The relative term adjusts the voltage vector grounded on the current error, whereas the integral term corrects for any steady-state deviations. These voltage vectors are fed into the PWM system to generate the necessary switching signals for the inverter, which produces an AC output with reduced harmonic distortion.

The PI controllers ensure precise tracking of reference power values and minimize inverter ripple, enhancing both steady-state and active execution. The control strategy uses present feedback and grid voltage feedforward loops to obtain stability and responsiveness to changing grid conditions. In grid-connected mode, the system adjusts the magnitude and phase angle of the inverter current to deliver the specified active and reactive power, helping to keep the grid stable and reliable. The performance of the HDGS unit is assessed based on the outputs of the PV irradiance, WT, and battery, ensuring optimal utilization of the RES.

The detailed control strategy using PI controllers, as described in Equations (27) to (30), ensures effective management of active and reactive power flow in a hybrid distributed generation method. By regulating current and voltage vectors, the system maintains grid stability, minimizes power losses, and enhances overall system efficacy and reliability.

PI controllers $(PI_1\ to\ PI_8)$ play a key role in the control strategies of inverters, PVs, wind, batteries and fuel cells. Proper tuning of the PI controller is essential for achieving the desired work in terms of stability, efficacy, and power quality. RESs such as PVs and wind are inherently variable due to changing weather conditions. A PI controller must be finely tuned to respond quickly and accurately to these variations to maintain system stability. MGs often operate in combination with the main grid. Proper tuning ensures smooth transitions among grid-connected and islanded modes, maintaining stable operation during such transitions.

The microgrid needs to balance the power generated from the PV, wind, and fuel cells with the load demand and battery storage. A well-tuned PI controller helps manage this balance by adjusting the power output of each source and the charging/discharging rates of the battery. Efficient power flow management minimizes losses and

ensures that the generated renewable energy is utilized optimally. This is particularly important for maximizing the use of renewable resources and minimizing dependency on nonrenewable sources.

Fluctuations in renewable energy generation can cause voltage instability. A PI controller with C voltage regulation helps maintain voltage levels within acceptable limits, thus ensuring a stable power supply to the loads. Renewable energy sources and battery inverters can introduce harmonics into the microgrid. Proper tuning of the PI controller can help minimize these harmonics, thereby improving the overall power quality. The microgrid operates under varying load and generation conditions. A finely tuned PI controller of the inverter can adapt to these changes, ensuring consistent performance and reliability. Effective tuning enhances the controller's ability to reject disturbances caused by rapid changes in load or generation, retaining steady-state operation and minimizing transient effects. The PI controller manages the charging and discharging phases of the battery, ensuring that the SOC is maintained within safe limits. This prolongs the battery life and ensures its availability for peak shaving and load levelling. During transitions such as charging to discharging and vice versa, the PI controller ensures smooth operations without causing significant power fluctuations or stress on the battery.

In the PI controller gains, the proportional gain (Kp) determines the response speed of the regulator to changes in the error signal. A higher Kp results in a faster response but can lead to overshoot and instability if it is too high. A lower Kp results in a slower response but provides more strength. Integral gain (Ki) rejects the steady-state error by integrating the error over time. A higher Ki improves accuracy in reaching the desired setpoint but can cause a slower response and oscillations if it is too high. A lower Ki results in less accurate control but a more stable system.

PI controller tuning is essential for the effective operation of microgrids with diverse energy sources, such as PV, wind, fuel cells, and batteries. Proper tuning ensures system stability, optimizes power flow, enhances power quality, and provides robust performance under varying conditions. Given the complexity and dynamic nature of microgrids, advanced tuning methods and adaptive control strategies are often necessary to achieve optimal performance. In this hybrid, the SSC optimization algorithm is adopted for tuning the eight PI controllers.

In this work, the optimization of the PI controller gains is performed via the integral of the time-weighted squared error (ITSE) as the performance index. The objective function to minimize is the sum of the integrals of the squared errors, each weighted according to the respective PI controller. This weighted approach allows different controllers to be prioritized based on their importance or specific performance requirements. The ITSE performance index emphasizes error reduction over time, which leads to a faster and more stable response from the control system. By minimizing the ITSE, the active response and performance of the control system are greatly improved. The final objective function to be reduced is as follows:

$$F\,(obj) = w_1 \times\ ITSE_1 + w_2 \times\ ITSE_2 + \ldots\ + w_n \times\ ITSE_n \tag{26}$$

- w_i are the weights assigned to each ITSE term.
- where $ITSE_i$ is the integral of the time-weighted squared error for the ith PI controller.

This formulation ensures that the optimization process balances the performance across multiple controllers, leading to an overall improvement in system stability and response time. By tuning the PI controller gains to minimize this aggregated ITSE, the control system can achieve superior performance in managing dynamic responses and reducing steady-state errors. A hybrid SSC adopted is adopted for the precise tuning of proportional-integral (PI) controllers by reducing the fitness function evaluated from the microgrid system presented in Fig. 1. Results obtained with hybrid SSC is compared with existing algorithms from the literature.

Existing algorithms

1. Dandelion Optimizer Algorithm (DOA)[25]: DOA, inspired by the seed dispersal process of dandelions, focuses heavily on exploration, enabling it to find diverse solutions in the early stages of optimization. However, it may struggle with rapid convergence and exploitation, especially in later stages, where it can become less efficient in fine-tuning the optimal solution. The SCA and SHO effectively balances exploration and exploitation by controlling search agent movements using trigonometric functions, leading to faster convergence and with its cooperative hunting-inspired behaviour, also excels in improving exploitation and ensuring that search agents converge toward global optima more effectively.
2. Coati Optimization Algorithm (COA)[26]: COA is modelled after the social foraging behaviour of coatis, which promotes leader-following behaviour for enhanced exploration and exploitation. While COA performs well in dynamically balancing exploration and local refinement, it can sometimes be slower in convergence when handling complex, multi-modal functions. SCA's oscillatory nature, defined by sine and cosine functions, provides better-controlled movement, allowing it to traverse the search space efficiently and quickly fine-tune solutions. SHO's social behaviour allows for superior local search capabilities, leveraging both individual and collective decision-making to fine-tune the solutions with more accuracy.
3. Crayfish Optimization Algorithm (CFOA)[27]: CFOA is inspired by crayfish movement, where search agents simulate underwater navigation for both exploration and exploitation. While CFOA is good at exploring the search space in constrained environments, it has limitations in terms of the speed and precision required for final solution refinement. In contrast, SCA's controlled oscillations between exploration and exploitation phases result in a faster and more precise convergence.
4. Binary Waterwheel Plant Optimization (BWPO)[28]: BWPO is based on the energy dynamics of a waterwheel system and is primarily suited for binary optimization problems. It operates well within its domain but struggles with continuous optimization tasks, particularly those requiring more sophisticated search mech-

anisms. SCA and SHO, on the other hand, are designed to handle both binary and continuous search spaces more effectively. SCA's trigonometric foundation allows for continuous and controlled transitions between exploration and exploitation, making it more adaptable. SHO, by mimicking the dynamic social behavior of spotted hyenas, provides better exploration and exploitation capabilities, leading to faster and more reliable convergence in continuous, real-time applications.

5. Harris Hawk Optimization Algorithm (HHO)[29]: HHO, inspired by the cooperative hunting strategy of Harris hawks, offers strong adaptive capabilities with a dynamic balance between exploration and exploitation. HHO has shown impressive results in a variety of optimization tasks, especially those involving real-world, complex problems. While both SCA and SHO are competitive with HHO, SCA provides an easier implementation and faster convergence due to its simple mathematical foundation. SHO, with its group-based decision-making, offers even better exploitation than HHO in certain scenarios, ensuring that local optima are avoided, and the global optima are reached.
6. Ziegler-Nichols (ZN)[18]: The Ziegler-Nichols method is a classical approach to tuning PID controllers and is based on empirical rules. Although simple to implement, ZN often provides suboptimal performance, particularly in systems with non-linear dynamics or time-varying characteristics. SCA and SHO, being more advanced, offer much greater adaptability and precision in tuning control parameters. SCA's ability to oscillate through search spaces allows it to fine-tune parameters more effectively than ZN, while SHO's collective hunting strategy enables better precision in finding optimal gains for controllers in complex systems.

The Sine-Cosine Algorithm (SCA) and Spotted Hyena Optimizer (SHO) demonstrate superior performance compared to traditional and modern optimization algorithms like DOA, COA, CFOA, BWPO, HHO, and ZN. Both SCA and SHO show enhanced convergence speed, adaptability, and precision in dynamic, multi-dimensional problems, particularly in real-time system optimization and controller tuning. Their balance between exploration and exploitation allows them to find better solutions more efficiently than the other mentioned techniques, making them ideal for complex, continuous optimization tasks.

Hybrid optimization algorithm

Sine–cosine algorithm

The SCA is a population-based metaheuristic optimization algorithm induced by mathematical sine and cosine functions. It was offered to solve optimization problems by efficiently exploring and exploiting the search space to obtain the optimal solution. SCA starts by adjusting a population of candidate solutions randomly in the stated search space. Every candidate solution is a potential solution to the optimization problem.

The positions of the candidate solutions are updated via sine and cosine functions, which allow the algorithm to explore and exploit the search space effectively[32].

$$SX_i^{k+1} = SX_i^k + R_1 \times \ sin\,(R_2) \times \ \left|R_3\,.PX_i^k - SX_i^t\right| \tag{27}$$

$$X_i^{k+1} = SX_i^k + R_1 \times \ cos\,(R_2) \times \ \left|R_3\,.PX_i^k - SX_i^t\right| \tag{28}$$

Equations 27 and 28 are used to update the solution's position by utilizing the oscillatory behaviour of the sine and cosine functions. These equations ensure that the solution moves closer to or farther from a target solution based on random parameters. Equation 27 utilizes the sine function to guide the solution's movement. Here, SX_i^k represents the current position of the solution, and PX_i^k is the position of the destination or target point, which can be the best-known solution or another agent. The difference $\left|R_3\,.PX_i^k - SX_i^t\right|$ calculates the absolute distance between the current solution and the target. This distance is modulated by R_3, a random factor that introduces stochastic behaviour into the search process, either emphasizing or deemphasizing the target's influence. The term $sin\,(R_2)$ determines the direction and amplitude of the movement, allowing the solution to oscillate around the destination. R_1 further scales the magnitude of the movement, allowing the algorithm to control aggressiveness of the solution movement. This update mechanism based on sine ensures that the solution explores both locally and globally.

In Eq. 28, the cosine function replaces the sine function to provide diversity in the movement pattern. While sine and cosine functions are similar in nature, the cosine function introduces a phase shift of 90 degrees, leading to a different directional exploration. The parameters R_1, R_2, and R_3 maintain their roles from the first equation, where R_1 scales the movement, R_2 adjusts the movement direction, and R_3 modulates the influence of the target. The cosine function's behaviour ensures that the solution is repositioned in a different region of the search space, complementing the sine-based exploration by searching in areas that may not be covered by the sine function alone. This phase difference between sine and cosine allows for more thorough coverage of the search space, reducing the likelihood of getting trapped in local optima.

Together, Eqs 27 and 28 form the core of the Sine Cosine Algorithm's update strategy. By alternating between sine and cosine functions, the algorithm ensures that the solution moves dynamically within the search space, effectively exploring and exploiting the environment to find optimal solutions. The combination of these cyclic functions with random scaling factors helps maintain a balance between local search (exploitation) and global search (exploration), making the SCA a versatile optimization tool.

In the early stage of the algorithm, larger steps (governed by R_1) ensure that the algorithm explores a broad area of the search space. As the algorithm continues, R_1 decreases, causing the steps to decrease and assisting the algorithm in fine-tuning the solutions around the promising areas found in the exploration phase. The fitness of each candidate solution is assessed by a predefined objective function specific to the optimization problem at hand. The best candidate result in terms of fitness is identified and updated as the best position.

The algorithm iterates, updating the positions of the candidate solutions via sine and cosine functions until a stopping criterion is met. Common stopping norms involve a maximum number of repetitions or a satisfactory fitness level. The algorithm outputs the best solution found during the iterations, which is deemed the optimal solution to the optimization problem.

Spotted Hyena Optimizer (SHO)

The SHO algorithm is a metaheuristic optimization technique advanced by the hunting activities and social hierarchy of spotted hyenas. This algorithm mimics the collaborative hunting strategies and social interactions observed in hyena packs to efficiently solve optimization problems. In nature, spotted hyenas hunt in packs and exhibit a complex social structure. Similarly, in SHO, the optimization process is driven by a population of candidate solutions, which can be viewed as members of a pack.

Hyenas collaborate during hunts, using strategies such as cooperative hunting, information sharing, and coordinated attacks. In SHO, this behavior translates into the exchange of information among candidate solutions (individual hyenas) to enhance the exploration and exploitation of the search space. Within a hyena pack, dominant individuals often lead and coordinate the group's actions. In SHO, leadership roles are assigned to promising solutions (leaders), which guide the exploration and exploitation phases. Communication among individuals (candidate solutions) facilitates the sharing of knowledge and experiences, analogous to how hyenas share information while they hunt.

The movement of candidate solutions in SHO is led by a set of rules that emulate the navigation and adaptation of hyenas in their environment. These rules govern how candidate solutions update their locations in the search space based on the collective knowledge of the pack (population). The fitness of each candidate solution is assessed by a predefined objective function that expresses the quality of a solution in relation to the optimization problem. This evaluation determines the success of a candidate solution (hyena) in the optimization process.

SHO iterates through multiple generations (epochs), where candidate solutions evolve and adapt based on their interactions and the guidance of leaders. The algorithm continues until a stopping criterion is met, such as a maximum number of repetitions of solutions to a satisfactory level.

The encircling behavior in the SHO is represented through a subsequent series of equations[50].

$$\overrightarrow{X_h} = \left| \overrightarrow{A} . \overrightarrow{C_P}(X) - \overrightarrow{C}\ (X) \right| \tag{29}$$

$$\overrightarrow{C}\ (X+1) = \overrightarrow{C_P}(X) - \overrightarrow{B}.\overrightarrow{X_h} \tag{30}$$

The distance traveled by a spotted hyena to access its prey is denoted as $\overrightarrow{X_h}$. The current repetition is indicated by x. $\overrightarrow{C_P}$ and $\overrightarrow{C}$ are the location vectors for the prey and the spotted hyena, respectively. The symbols · and || are the multiplication vectors and absolute values, respectively. The coefficient vectors $\overrightarrow{A}$ and $\overrightarrow{B}$ are computed as follows[50]:

$$\overrightarrow{A} = 2.x\ \overrightarrow{d_1} \tag{31}$$

$$\overrightarrow{B} = 2\ \overrightarrow{h}\ .x\ \overrightarrow{d_2} - \overrightarrow{h} \tag{32}$$

$$\overrightarrow{h} = 5 - \left(Itr \times \frac{5}{Max_{ltr}} \right) \tag{33}$$

where itr = 0,1, 2…., Max_{ltr}

In every repetition, the value of $\overrightarrow{h}$ decreases from 5 to 0. The random vectors $x\overrightarrow{d_1}$ and $x\overrightarrow{d_2}$ take on values within the range of [0, 1]. Modifying the location vectors $\overrightarrow{A}$ and $\overrightarrow{B}$ enables exploration of different positions. Additionally, by employing the following equations, the hunting manners of hyenas are simulated, allowing for the identification of potential hunting regions[50].

$$\overrightarrow{X}_h = \left| \overrightarrow{A}\ .\ \overrightarrow{C}_h - \overrightarrow{C}_k \right| \tag{34}$$

$$\overrightarrow{C}_k = \overrightarrow{C}_h - \overrightarrow{B}.\overrightarrow{X}_h \tag{35}$$

$$\overrightarrow{O}_h = \overrightarrow{C}_k + \overrightarrow{C}_{k+1} + \ldots, + \overrightarrow{C}_{k+N} \tag{36}$$

N is the number of iterations, which can be computed as follows[50]:

$$N = Count_{nos}\ \left(\overrightarrow{C}_h, \overrightarrow{C}_{h+1}, \overrightarrow{C}_{h+2}, \ldots, \left(\overrightarrow{C}_h + \overrightarrow{M} \right) \right) \tag{37}$$

$$\overrightarrow{C}\ (X+1) = \frac{\overrightarrow{O}_h}{N} \tag{38}$$

The operation phase of the SHO algorithm commences when the magnitude of $\overrightarrow{B}$ is less than 1, and it is initialized randomly within the range of [-1, 1]. In the SHO process, the optimization process begins by generating a populace of random solutions. Initially, the search agents cluster together by revealing the positions of the top-performing agents and subsequently adjusting their positions. In each iteration, the factors h and E

linearly decrease. Once iteration is successfully completed, the best positions associated with the search agents are retrieved[51].

Chimp Optimization Algorithm (ChoA)

The COA is a metaheuristic optimization technique taught by the characteristics of chimpanzees, particularly their foraging and social interaction strategies[52]. This algorithm models the search and exploration behaviors observed in chimpanzees to efficiently solve optimization problems. The COA starts by creating a population of candidate solutions, which are potential answers to the optimization problem. These candidate solutions can be likened to individual chimpanzees within a group. Chimpanzees exhibit intelligent foraging behaviors where they explore their environment for food sources. Similarly, in COA, candidate solutions explore the search space to locate optimal results by iteratively adjusting their places.

Chimpanzees learn from each other and share information within their social groups. The COA incorporates social learning mechanisms where candidate solutions exchange information (knowledge sharing) to improve their solutions collectively. This interaction helps in exploiting promising regions of the search space. Within a chimpanzee group, leaders often emerge since their experience and success in finding resources. The COA employs leader–follower dynamics, where certain candidate solutions (leaders) guide the exploration and exploitation stage of the process. Followers learn from leaders and adjust their search behaviors accordingly.

The fitness of each candidate solution is assessed by an actual function specific to the optimization problem. This function quantifies how well a candidate solution performs relative to the problem's requirements or constraints. The COA iterates through multiple generations (epochs), where candidate solutions evolve and adapt based on their interactions and guidance from leaders. The algorithm continues until a stopping norm is met, such as a maximum number of iterations to obtain a satisfactory solution.

The exact replica of the algorithm is as follows[52]:

$$D_r = |c\,.a_{prey}\,(n_i) - ma_{chimp}\,(n_i)| \tag{39}$$

$$a_{chimp}\,(n_i + 1) = a_{prey} - a.d \tag{40}$$

The coefficients used in the algorithm, namely, c, m, and a, are determined through the resulting equations. The sum of iterations is denoted by n_i[52].

$$a = 2.l.r_1 - l \tag{41}$$

$$c = 2\,.r_2 \tag{42}$$

$$m = chaotic_{value} \tag{43}$$

The factors c, m, and a are estimated via the following equations, where $r_1\ and\ r_2$ is a random number in the range [0, 1]. The chaotic vector m is also involved in the calculations. Additionally, in the iteration process, the value of l is gradually decreased from 2.5 to 0[52].

$$d_{attacker} = |c_1 a_{attacker} - m_1\,.x| \tag{44}$$

$$d_{barrier} = |c_2 a_{barrier} - m_2\,.x| \tag{45}$$

$$d_{chaser} = |c_3 a_{chaser} - m_3\,.x| \tag{46}$$

$$d_{driver} = |c_4 a_{driver} - m_4\,.x| \tag{47}$$

If the random vectors fall in the range of [-1, 1], the next position of the chimp can be found in its current location and the position of the target or prey[52].

$$x_1 = a_{attacker} - a_1.d_{attacker} \tag{48}$$

$$x_2 = a_{barrier} - a_2.d_{barrier} \tag{49}$$

$$x_3 = a_{chaser} - a_3.d_{chaser} \tag{50}$$

$$x_4 = a_{driver} - a_4.d_{driver} \tag{51}$$

The chimp's location is modified during the search via the following mathematical equation[52].

$$x_{n_i+1} = \frac{x_1+x_2+x_3+x_4}{4} \tag{52}$$

In the search method in the search domain, the chimp's location is updated via the following mathematical equation[52].

$$a_{chimp}\ (n_i + 1)\ = \begin{cases} a_{prey}\,(n_i) - x.d & if\ \varnothing\ < 0.5 \\ chaotic_{value} & if\ \varnothing\ > 0.5 \end{cases} \tag{53}$$

Hybrid SSC

In the realm of metaheuristic optimization, tackling complex problems poses a significant challenge, as no single algorithm consistently outperforms others across all scenarios. Each approach has its limitations when confronted with intricate functions, necessitating efficient strategies capable of effectively balancing exploration and exploitation processes. To address this need, we propose an advanced algorithm that integrates sine–cosine function dynamics with the attacking strategy inspired by Spotted Hyena Optimization (SHO). This enhanced methodology builds upon the initial steps of the Chimp Optimization Algorithm (COA), which aims to provide robust solutions for complex optimization functions in competitive environments.

The algorithm harnesses the dynamic properties of sine and cosine functions to enhance its ability to locate optimal solutions amid complex optimization landscapes. These functions play a pivotal role in steering the algorithm away from local optima, thereby facilitating exploration toward global optima. In contrast, the Chimp optimization algorithm (ChoA), while proficient in solving numerous complex optimization problems, grapples with challenges in navigating the search space, often becoming ensnared in local optima and struggling to reach global optimum values. These limitations become more pronounced in larger and more intricate optimization scenarios, where issues such as impulsive convergence, lack of range, and slow convergence rates hinder performance.

To address these shortcomings, significant modifications have been introduced to augment the algorithm's search capabilities within the domain. These adaptations are specifically tailored to accurately identify and converge upon global optimum solutions for complex optimization functions, thereby enhancing overall performance. The original phases of the chimp optimization algorithm have been restructured to streamline the discovery process of optimal solutions, whereas the newly implemented phases focus on leveraging discovered optima within the search domain. This strategic adjustment has notably expedited the achievement of optimal global performance while effectively mitigating the influence of local optima.

As a result of these refinements, the convergence rate of the original ChoA algorithm has markedly improved. By integrating enhanced search strategies and optimizing the utilization of sine and cosine functions, the algorithm now demonstrates heightened efficiency in navigating complex optimization landscapes, surpassing previous limitations and bolstering its applicability across diverse problem domains.

The hybrid SSC algorithm is mathematically formulated through a series of structured steps, each aimed at efficiently navigating and optimizing within a complex search space.

- The algorithm starts by initializing a population of search agents, represented as chimaps in this analogy. Each chimp (search agent) is assigned a randomly initialized n-dimensional vector denoted as X_i (where i = 1, 2., n). This vector is the position of all search agents in the search space.
- In the next step, each search agent (chimp) evaluates its location in the search space built on a predefined objective function. The objective function measures the performance or fitness of each chimp's position relative to the optimization problem's goals. The fitness value indicates how well the result represented by X_i satisfies the optimization criteria.
- During the exploration phase, chimps update their positions in the search space to obtain optimal solutions. This renewal mechanism allows the search agents to navigate toward potentially better positions that improve their fitness scores. The exploration phase is crucial for discovering new promising solutions and avoiding local optima.
- The algorithm incorporates a hybrid SSC technique, which combines the principles of sliding surface control to dynamically adjust the search direction based on the current state and the desired trajectory. This strategy helps efficiently guide the search agents toward optimal solutions by balancing exploration (searching new areas) and exploitation (improving existing solutions).
- Through iterative updates and evaluations, the algorithm aims to converge toward optimal solutions within the complex search space. By continuously updating positions based on fitness evaluations and optimizing the search trajectory via hybrid SSC techniques, the algorithm enhances its efficiency in finding high-quality solutions[40].

$$r_2 = (2\pi) \times rand \tag{54}$$

$$x_1 = a_{attacker} - cos(r_2) \times a_1.d_{attacker}$$

$$x_2 = a_{barrier} - sin(r_2) \times a_2.d_{barrier}$$

$$x_3 = a_{chaser} - cos(r_2) \times a_3.d_{chaser}$$

$$x_4 = a_{driver} - cos(r_2) \times a_4.d_{driver}$$

where r_2 is a random number in the range of [0, 1].

- Stopping conditions were set to determine when to end the search process and find the chosen optimal value. These situations help choose the best search agents in the population and allow for their replacement based on the performance of the top search agent. The iteration method is repeated until the stopping criterion is met, which could include reaching the maximum allowable number of iterations or finding a solution within the desired timeframe.

Simulation results

In this section, simulation results that justify the efficacy of the HYBRID SSC optimization method for controlling an MG system are presented. The performance metrics include keeping the DC bus voltage stable and ensuring that the active and reactive powers remain within the stated ranges in various operating modes of the MG. The simulations were conducted via MATLAB/SIMULINK, and the system needs are detailed in Table 1. Table 1 summarizes the terms of the MG system used in the simulations. This includes details such as component ratings, control objectives, and operational modes considered during testing. To determine the control of the HYBRID SSC-based control strategy, a comparative analysis is performed against several other optimization algorithms commonly used in control strategies for MG systems. These include:

1. Dandelion optimizer algorithm (DOA)[25].
2. Coati Optimization Algorithm (COA)[26].
3. Crayfish optimization algorithm (CFOA)[27].
4. Binary Waterwheel Plant Optimization (BWPO)[28].
5. Harris Hawk Optimization Algorithm (HHO)[29].
6. Ziegler–Nichols (ZN)[18].

The control program drawn in Sect. 3 is applied to the optimized PI gains obtained through the hybrid SSC algorithm. These gains are key for ensuring the stability and performance of the MG system in different operational states.

- Case 1: Reference active and reactive power change: Evaluates the system's response to variations in reference active and reactive power setpoints, ensuring accurate tracking and stability.
- Case 2: Isolation of PV and wind generation systems: Changes in solar irradiance and wind speed are simulated to evaluate the robustness of the control strategy for varying renewable energy inputs. In addition, we investigate the performance when PV and wind generation systems operate independently, reflecting real-world scenarios.
- Case 3: Real-time data of irradiance and wind speed: Data inputs to the PV and wind generation system are collected in real-time, and the data system response is evaluated.

Table 2 presents the optimization parameters required by the algorithm hybrid SSC. Table 3 presents the PI gains optimized by the hybrid SSC algorithm for control of the MG system. These gains are compared against gains optimized by other algorithms from the literature, demonstrating the effectiveness of hybrid SSC in achieving optimal control performance. The simulation results demonstrate the ability of the hybrid SSC algorithm-based control method to state the DC bus voltage within the needed limits under varying load conditions and renewable energy inputs. Effective control of the active and reactive powers is achieved, ensuring grid stability and efficient energy management across different operational modes of the MG. Through comparative analysis, it is shown that the Hybrid SSC algorithm outperforms other optimization techniques in terms of merging speed, precision, and robustness in achieving optimal PI gains for the control strategy.

The simulation outcomes validate the efficacy in maintaining stable operation of the MG system. By optimizing the PI gains and demonstrating superior performance compared with existing methods, hybrid SSC proves to be a robust solution for enhancing the grid integration of the RES and reliable MG operation. These

PV Array	
Series connected modules	5
Parallel Strings	66
Maximum Power of Module	305 W
Open Circuit Voltage (V_{oc})	64.2 V
Short Circuit Current (I_{sc})	5.96 A
MPP voltage (V_{mpp})	54.7 V
MPP Current (I_{mpp})	5.58 A
Wind Turbine and PMSG	
Base Wind Speed	8 m/s
Nominal mechanical output power	50 kW
PMSG Stator Resistance and Inductance	0.425 ohm and 8.5 mH
Torque constant and inertia	3.2475 and 0.01197 kg.m2
Fuel Cell	
Power and Voltage	10 kW and 45 Vdc
Battery	
Nominal Voltage	500 V
Rated Capacity	600 Ah

Table 1. System parameters.

Parameter	Value
Dimensions of the problem	16 ($K_{p1},\ K_{p2}, \ldots ,\ K_{p8}$), ($K_{i1},\ K_{i2}, \ldots ,\ K_{i8}$)
Number of search agents	50
Number of iterations	100
$R_1,\ R_2,\ R_3$ and $r_1,\ r_2,\ r_3$ and r_4	Random numbers within the range [0,1]
Fitness Function	$w_1 \times\ ITSE_1 + w_2 \times\ ITSE_2 + \ldots + w_8 \times\ ITSE_8$
w coefficient in fitness function	1/8
$ITSE$	Integrated Time Squared Error of PI controller

Table 2. Optimization parameters of hybrid SSC algorithm.

Algorithm	$K_{p1},\ K_{i1}$	$K_{p2},\ K_{i2}$	K_{p3}, K_{i3}	K_{p4}, K_{i4}	K_{p5}, K_{i5}	K_{p6}, K_{i6}	K_{p7}, K_{i7}	$K_{p8},\ K_{i8}$
Proposed HSSC	0.2358, 1.1542	0.5418, 5.6726	0.5469, 0.8347	0.8003, 3.2548	0.0357, 1.5538	0.0357, 1.5538	0.8235, 2.0978	0.8235, 2.0978
DOA	0.1764, 5.1173	0.2344, 6.5621	0.4854, 1.3567	0.7922, 3.3921	0.0483, 4.6297	0.0483, 4.6297	0.9502, 5.0384	0.9502, 5.0384
COA	0.2098, 6.6647	0.8754, 3.2755	0.4218, 1.1267	0.7577, 3.0687	0.0187, 2.8675	0.0187, 2.8675	1.1687, 5.3275	1.1687, 5.3275
CFOA	0.2371, 5.3752	0.3876, 5.2278	0.3522, 1.9657	0.607, 5.8132	0.0375, 3.3674	0.0375, 3.3674	1.1168, 4.5867	1.1168, 4.5867
BWPO	0.0687, 7.0698	0.3587, 7.5379	0.5388, 2.0876	0.7534, 4.6237	0.0976, 3.3675	0.0976, 3.3675	0.7028, 5.0875	0.7028, 5.0875
HHO	0.1359, 3.6758	1.1687, 3.4879	0.7382, 3.6489	0.6958, 3.5684	0.0486, 2.0869	0.0486, 2.0869	0.7395, 3.1875	0.7395, 3.1875
Ziegler Nicholas	1.2237, 8.9324	2.6675, 8.5478	1.3584, 10.365	1.9547, 12.398	0.0538, 7.0872	0.0538, 7.0872	1.3387, 8.6924	1.3387, 8.6924

Table 3. Optimized gains of the PI controllers via the proposed algorithm and various other algorithms.

findings underscore the potential of hybrid SSC in advancing control methodologies for future smart grids and RESs.

Case 1

In this case, active changes in the active and reactive power references are analyzed over specific time intervals. The change is as follows:

- From 0 to 4 s, P_{ref} is 170 kW, and Q_{ref} is 120 kVAR.
- From 4 to 8 s, P_{ref} is increased to 150 kW, and Q_{ref} is increased to 90 kVAR.
- From 8 to 12 s, P_{ref} decreases to 120 kW, and Q_{ref} decreases to 80 kVAR.
- 12 to 16 s, P_{ref} changes to 135 kW and Q_{ref} to 75 kVAR.
- From 16 to 20 s, P_{ref} stabilizes at 160 kW, and Q_{ref} stabilizes at 105 kVAR.

Throughout this period, the connected load remains unchanged at 250 kW and 180 kVAR, creating a consistent demand on the system. The PV system receives 1000 W/m² of sunlight at a temperature of 35 °C, and the wind generation system operates under a wind speed of 12 m/s. Figure 9 illustrates the changes in irradiance, temperature, and wind speed over time, while Fig. 10 provides a comparison of the microgrid's power tracking efficiency using optimized PI controller gains derived from the hybrid sine-cosine and spotted hyena-based chimp optimization algorithm (HSSC). The performance of this optimized algorithm is compared with other optimization techniques, including the DOA, COA, CFOA, BWPO, HHO, and the classical Ziegler–Nichols (ZN) method.

The performance analysis continues with visualizations of active and reactive powers. Figures 11 and 12 capture the power injected by the microgrid between 0 and 1 s and 7.9 to 9 s, respectively. These intervals are chosen to highlight the dynamic responses during significant shifts in power demand and control adjustments. Additionally, Fig. 13 illustrates the active and reactive power supplied to the load by the microgrid, providing insight into the effectiveness of the control strategy. Figure 14 outlines the power provided by the grid to supplement the microgrid when the demand exceeds the microgrid's generation capacity. Between 0 and 4 s, for instance, the microgrid delivers 170 kW and 120 kVAR, matching its reference values. However, the load's total requirement is 250 kW and 180 kVAR, meaning that the grid must supply the shortfall of 80 kW and 60 kVAR.

The power generation contributions from various sources, including PV, wind, and fuel cells, are depicted in Fig. 15, along with the available power at the battery terminals. At full irradiance and optimal wind conditions, the total power generated by these renewable sources is 158.89 kW. In the intervals from 0 to 8 s and from 16 to 20 s, the reference power demand exceeds the generated power. To balance the system, the battery discharges to supply the necessary excess power. Between 8 and 16 s, however, the generation from renewable sources exceeds the demand, causing the surplus power to be stored in the battery, which enters a charging mode during this period.

The state of charge (SOC) of the battery fluctuates based on the system's power dynamics, as shown in Fig. 16. During the charging phase (8 to 16 s), the SOC increases, indicating energy storage in the battery. Conversely, during the discharge phases (0 to 8 s and 16 to 20 s), the SOC decreases as the battery supplements the power

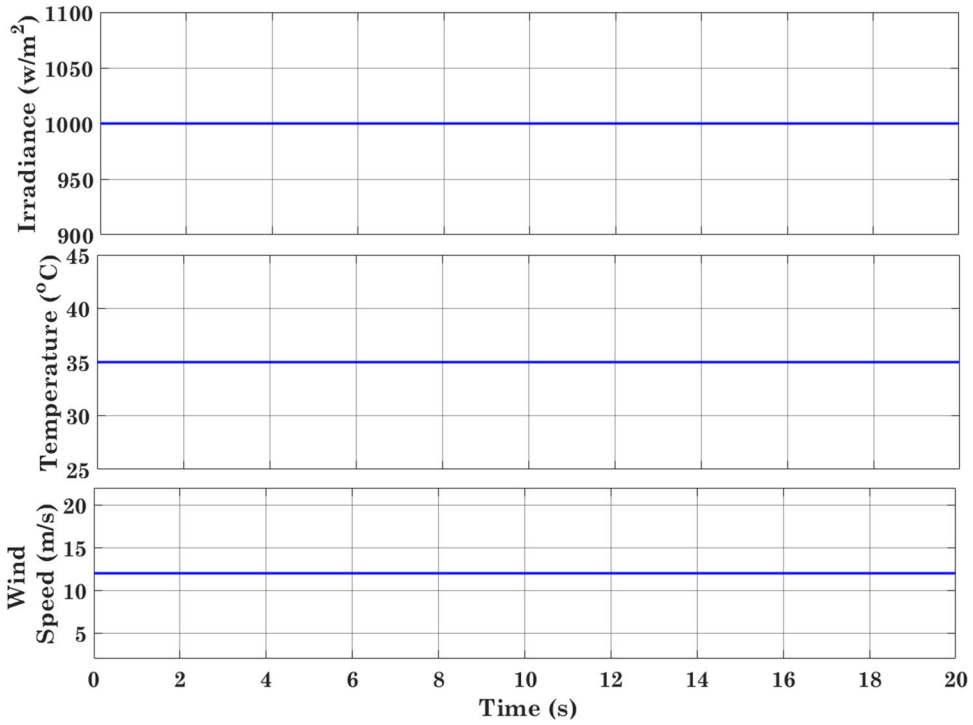

Figure 9. Irradiance, temperature and wind speed.

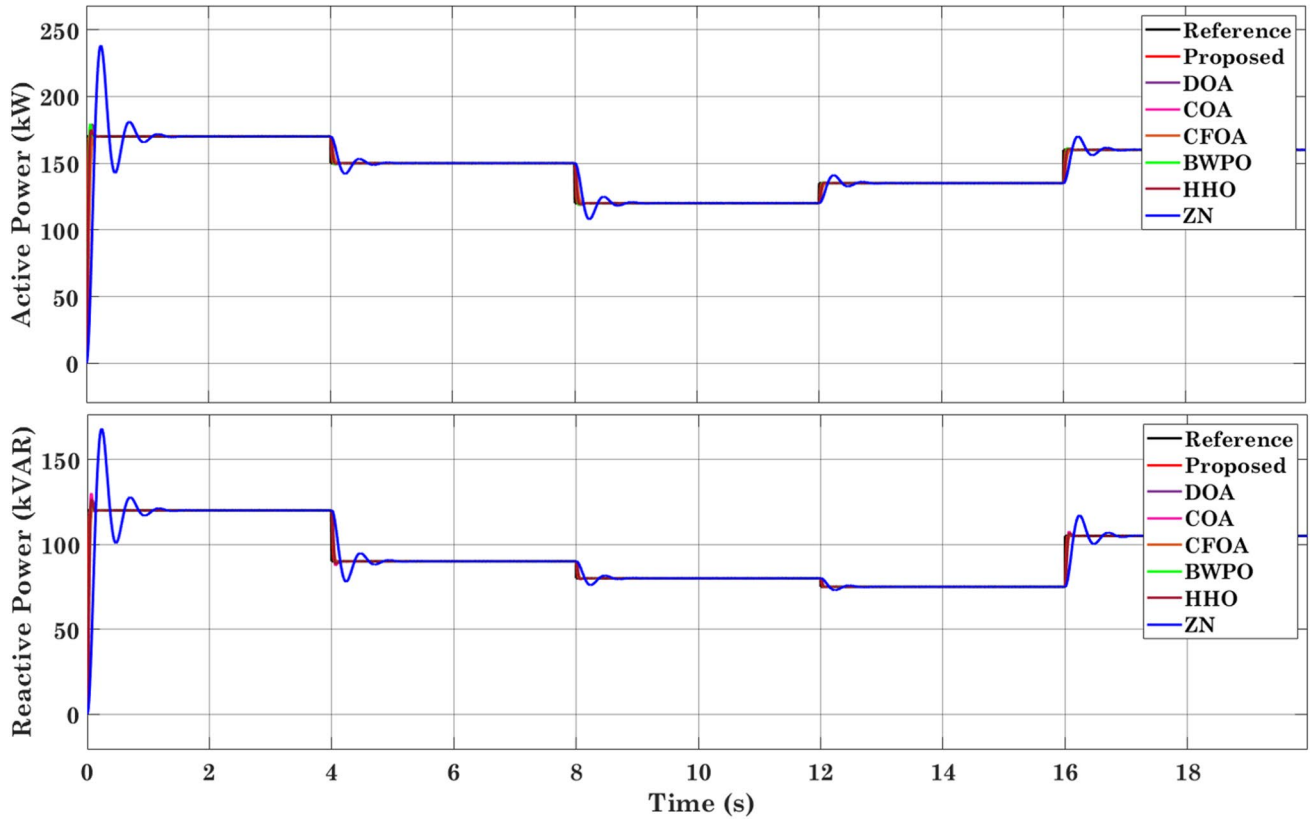

Figure 10. Comparison of tracking ability in active and reactive power generation by the microgrid using proposed and various optimization algorithms.

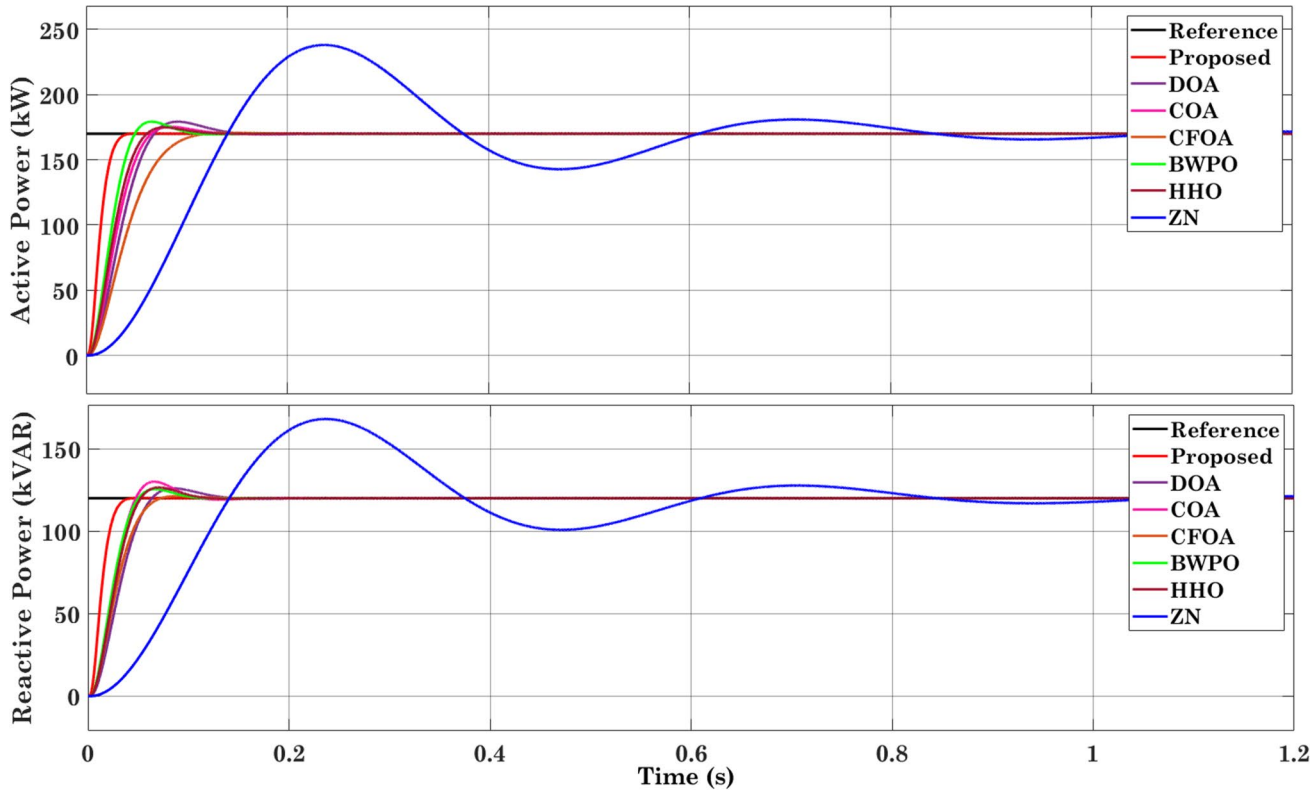

Figure 11. Active and reactive power generation from 0 to 1.2 s in kW.

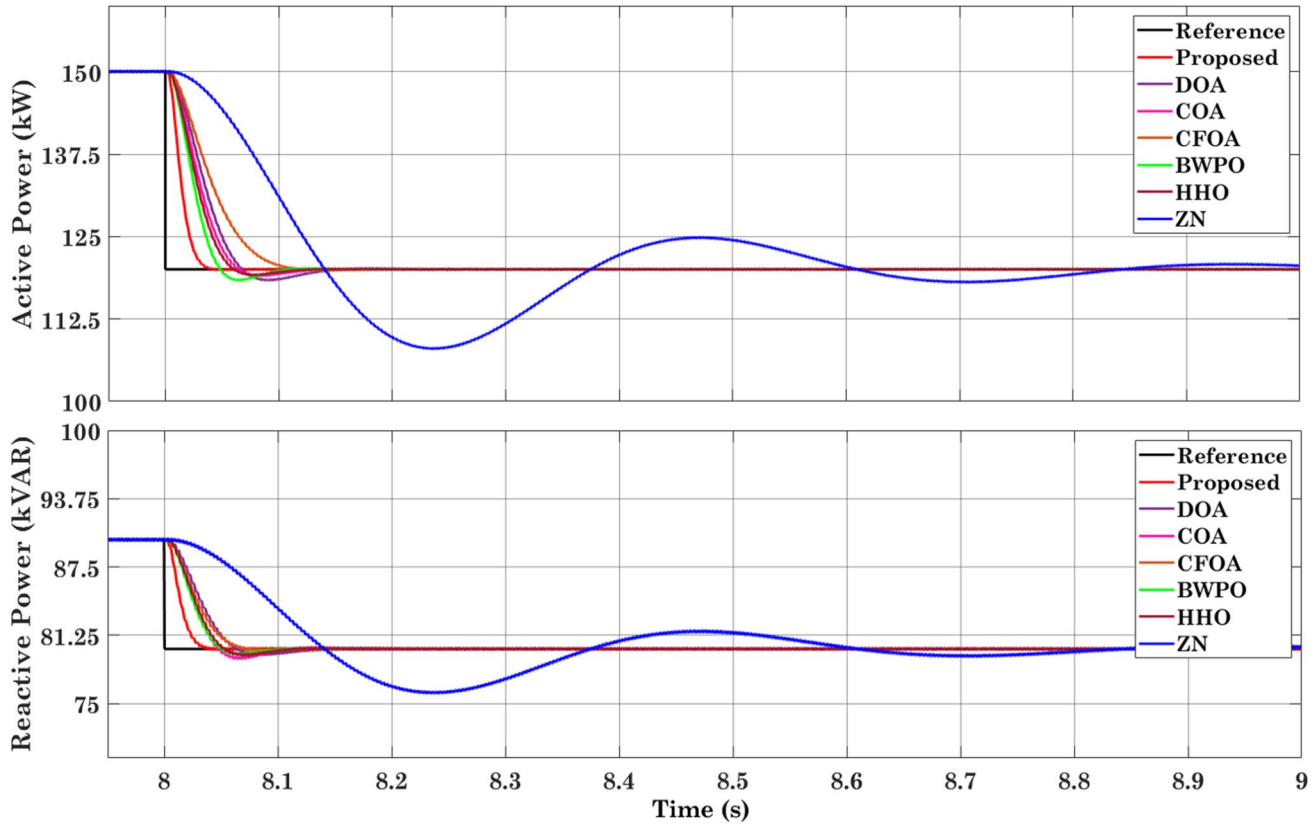

Figure 12. Active and reactive power generation from 7.9 to 9 s in kW.

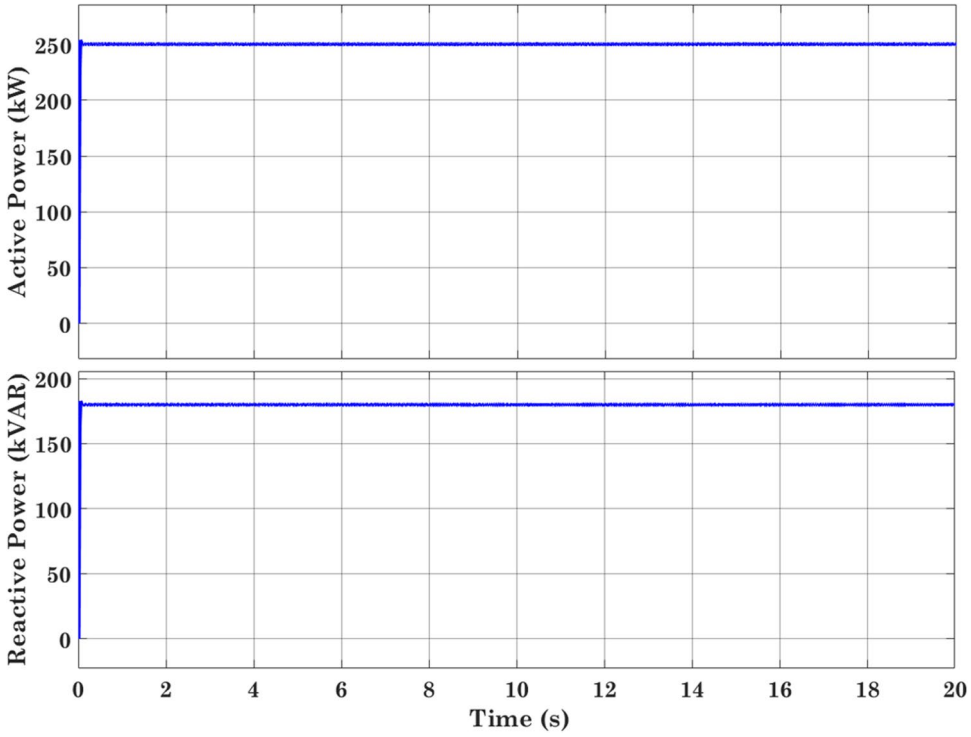

Figure 13. Load Active and Reactive power in kW.

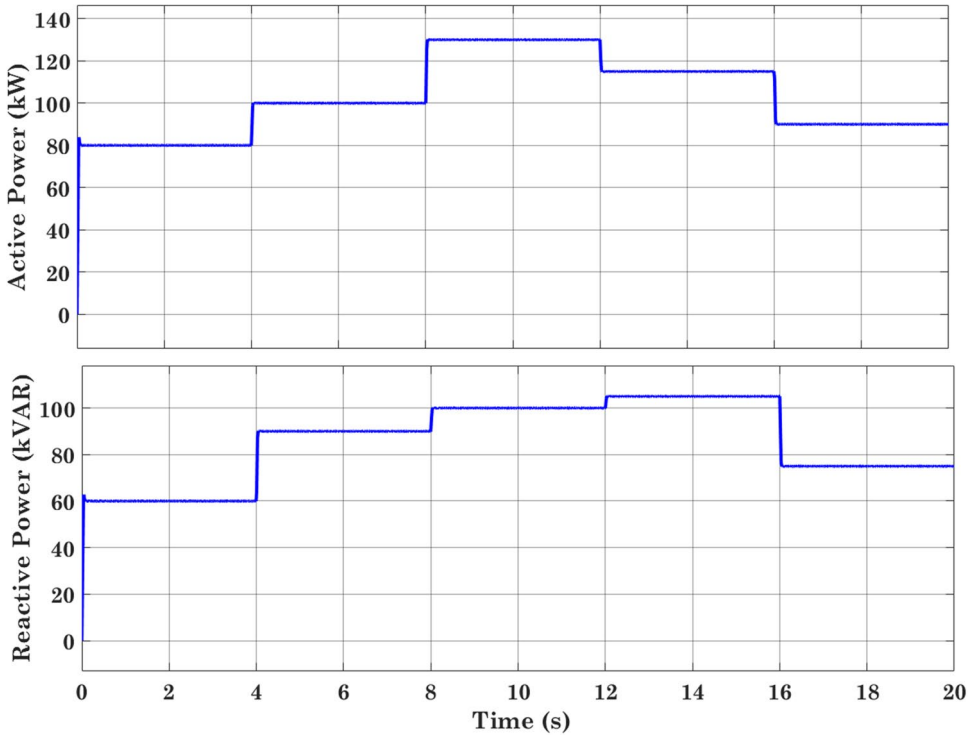

Figure 14. Grid active and reactive power in kW.

needed by the load. This cyclical operation of charging and discharging ensures the reliability and continuity of power supply, maintaining stability within the microgrid.

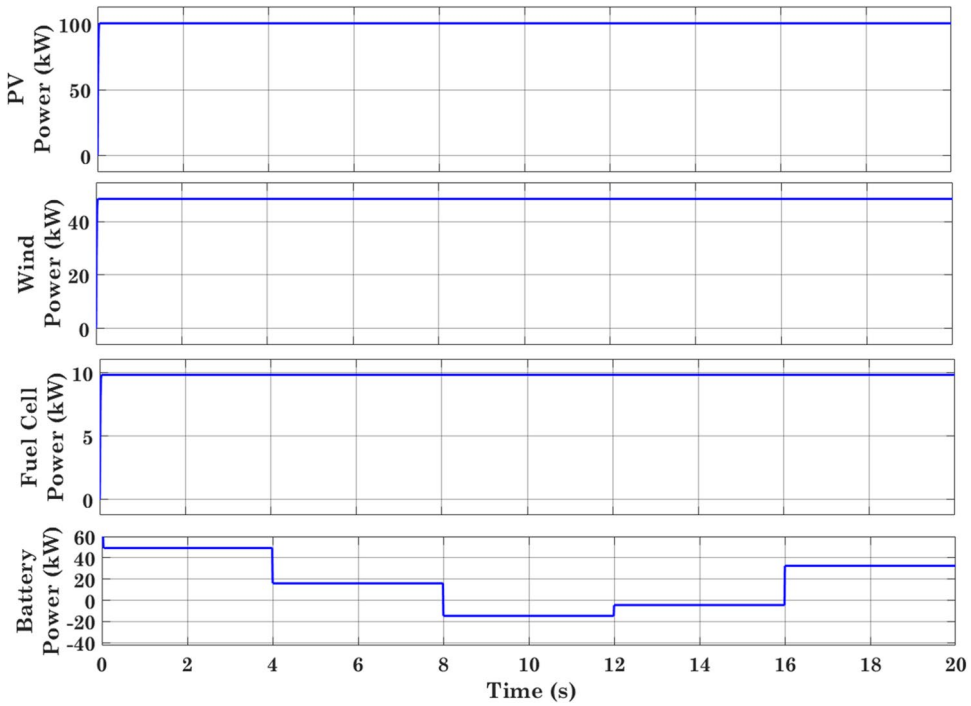

Figure 15. Power generated by the PV, wind, fuel and battery cells in kW.

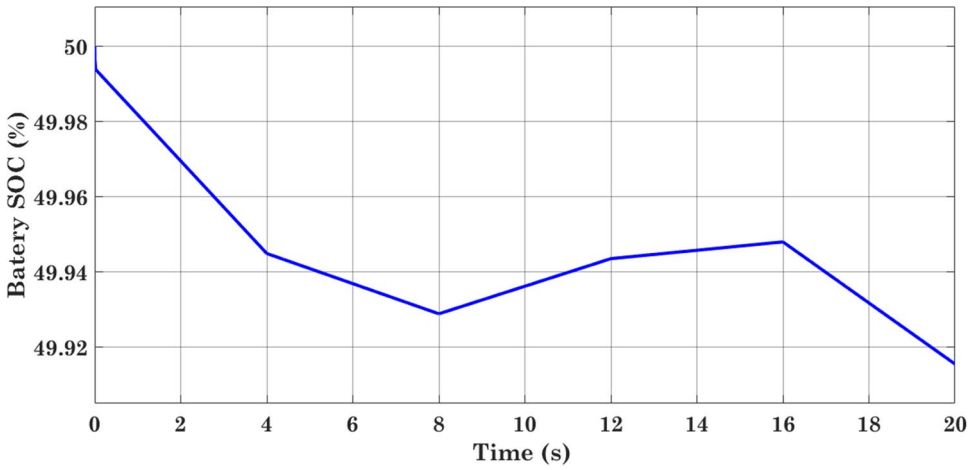

Figure 16. Battery SOC in %.

Case 2

The performance of the PI controllers, tuned by the proposed algorithm, is evaluated under conditions of variable irradiance and wind speed, as well as during scenarios where the PV and wind generation systems are isolated from the microgrid. In this case, the load remains constant at 250 kW for active power and 180 kVAR for reactive power. The control strategy is tasked with ensuring that the microgrid delivers target active and reactive power inputs of 180 kW and 150 kVAR, respectively, despite the fluctuating conditions. Figure 17 illustrates the variations in irradiance and wind speed over time, capturing the dynamic changes that challenge the stability of the power system. Figure 18 presents the power contributions from the PV, wind, fuel cell, and battery sources throughout the simulation.

During specific periods of the simulation, the PV and wind generation systems are intentionally isolated from the microgrid to assess the system's resilience. The PV generation system is disconnected from the microgrid from 4 to 12 s, and the wind generation system is isolated from 15 to 25 s. During these intervals, the power output from the respective sources drops to zero, creating a temporary power deficit. To ensure that the reference power values of 180 kW and 150 kVAR are still tracked effectively, the battery system steps in to compensate for the lost generation. As a result, the battery discharges, providing the additional power needed to maintain

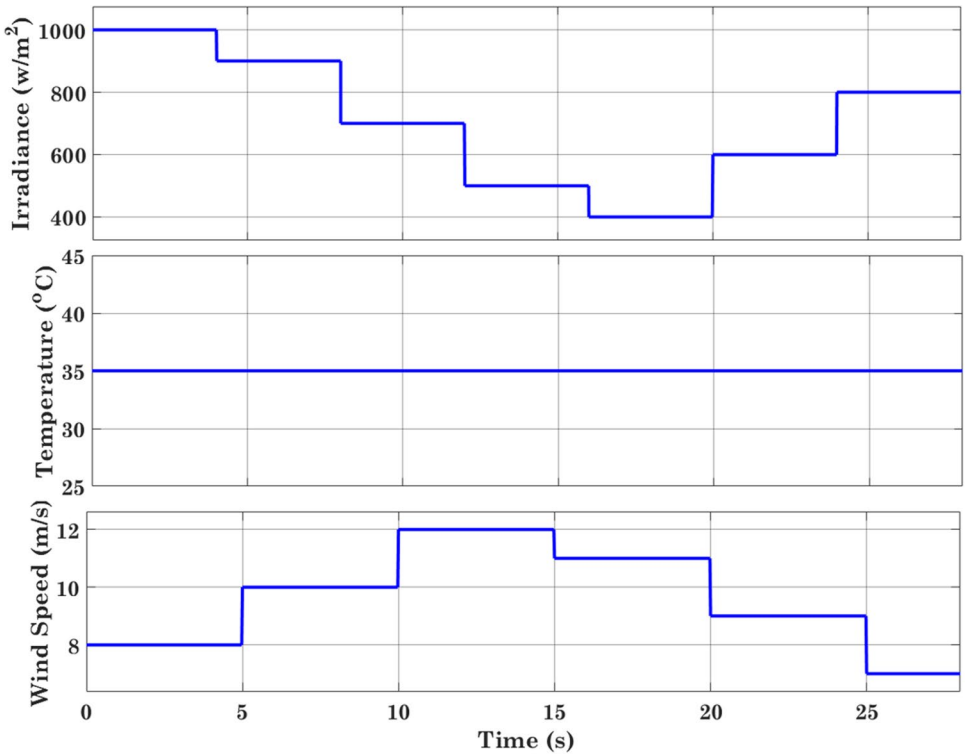

Figure 17. Variation in the irradiance, temperature and wind speed in case 2.

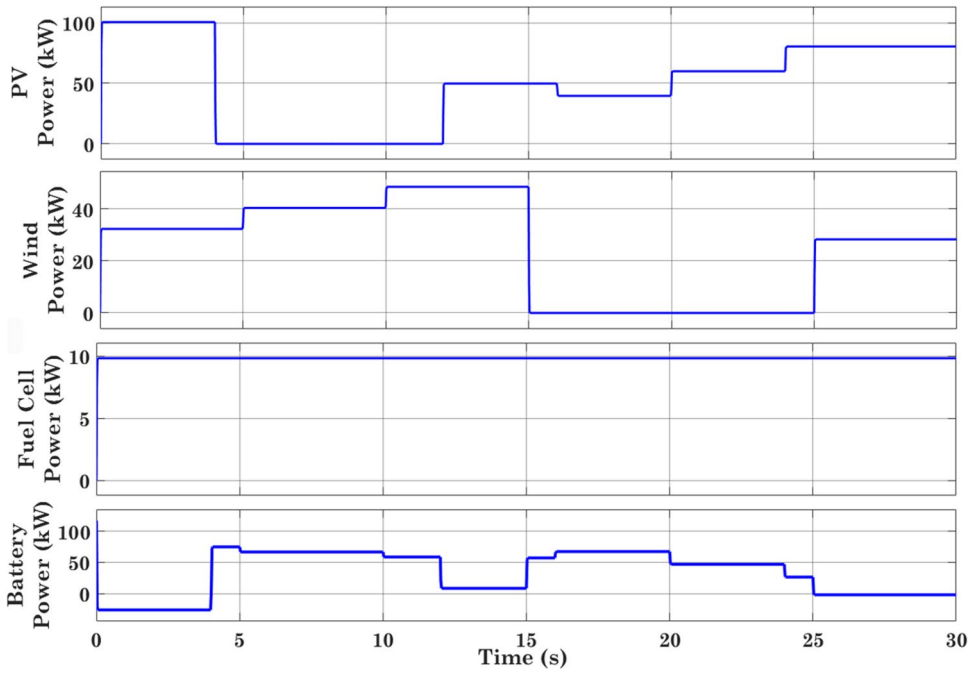

Figure 18. Power generated by the PV, wind, fuel and battery cells in kW.

system balance and meet the load demands. This is especially evident in the increased battery power output between 4 and 12 s and 15 to 25 s, where the battery takes on a critical role in maintaining the microgrid's stability and power supply.

The dynamic behavior of the battery during these isolation periods underscores its essential role in supporting the microgrid when renewable energy sources are temporarily unavailable. The battery acts as a buffer, discharging energy to compensate for the absence of generation from PV and wind sources, thereby

ensuring that the microgrid continues to operate smoothly. The effectiveness of the battery's response during these critical intervals highlights the importance of energy storage in maintaining the reliability of a microgrid, particularly under variable renewable energy inputs.

Figure 19 provides a detailed overview of the various power components within the microgrid system, offering a comprehensive visualization of how different sources interact to meet the load demands. It displays both the reference and actual powers associated with the inverter, along with the power generated by PV, wind, and fuel cell sources. Additionally, the power dynamics at the battery terminals are shown, indicating the battery's charging and discharging cycles as it compensates for fluctuations in renewable energy generation. Figure 19 includes the active and reactive powers supplied by both the grid and the load, demonstrating how the grid contributes to the overall system when the local generation and battery storage fall short. This in-depth depiction of power interactions within the microgrid reveals the system adaptation to varying conditions of irradiance and wind speed. The coordination between the inverter, battery, and grid ensures that the microgrid meets the load's demands efficiently and reliably, maintaining power quality and continuity throughout the simulation.

Case 3

Real-time data for irradiance, temperature, and wind speed were acquired from the National Solar Radiation Database (NSRD)[53] to evaluate the effectiveness of optimized PI controller gains in maintaining accurate tracking of active and reactive power standards within the microgrid. These real-time values, originally collected hourly, have been adapted for the simulation by considering second-by-second variations to provide a more granular analysis. Figure 20 visualizes the collected irradiance, temperature, and wind speed data over time, allowing a detailed examination of how these environmental factors fluctuate and influence the performance of the microgrid.

Figure 21 illustrates the power contributions from various generation sources, including photovoltaic (PV) panels, wind turbines, fuel cells, and battery storage. The figure provides a comprehensive overview of the total power output from each source, demonstrating coordination to meet the energy demands of the microgrid. Each source contributes differently based on the prevailing environmental conditions, such as irradiance, wind speed, and temperature, which directly affect the power generation capabilities of PV and wind systems. The fuel cell and battery storage systems also play pivotal roles in ensuring a continuous power supply, especially during periods when renewable energy generation fluctuates.

In Fig. 22, the power dynamics within the microgrid are depicted in detail. This figure presents both the reference and actual power values associated with the inverter, providing insights into the efficacy of the PI controllers, optimized by the proposed algorithm, track the desired power outputs. In addition to the inverter's performance, the figure also displays the generated powers from the PV, wind, and fuel cell systems, highlighting

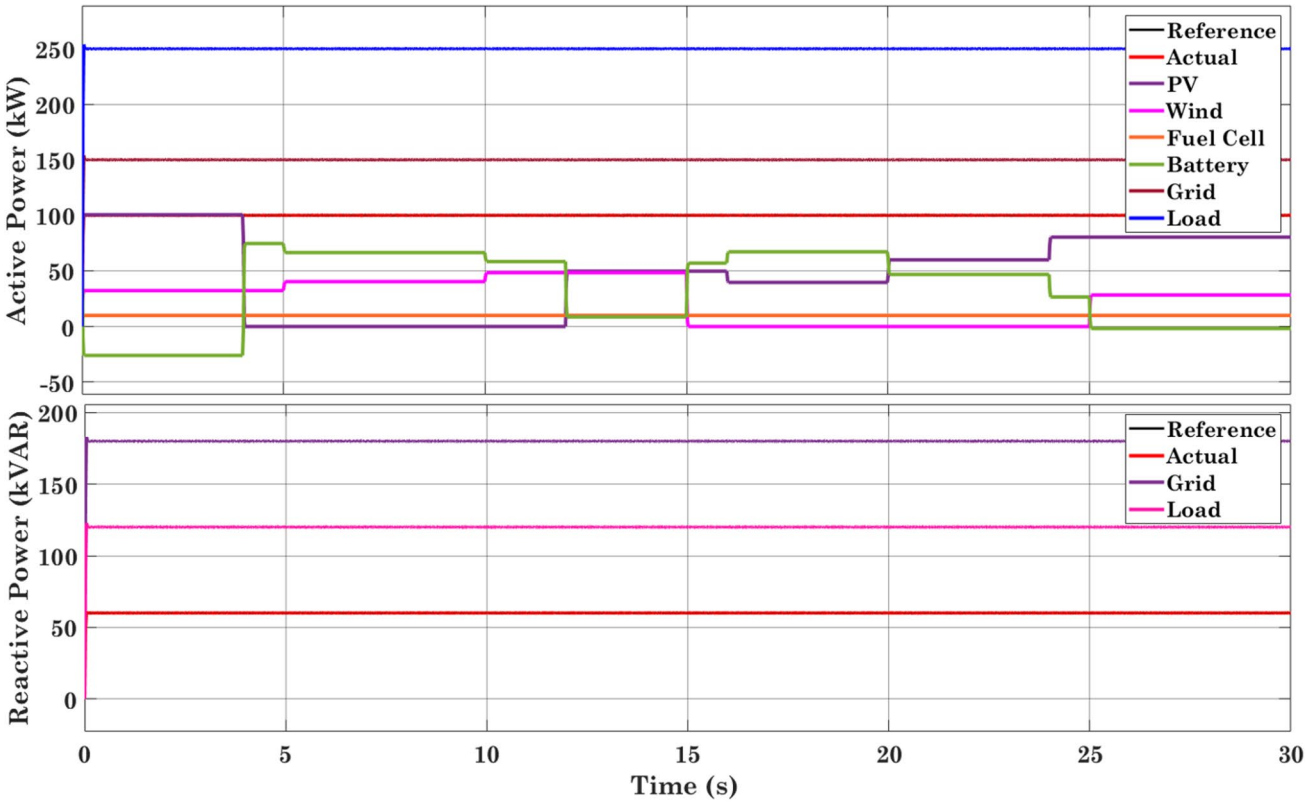

Figure 19. Reference and actual powers of the inverter, PV, wind and fuel cell-generated powers, battery terminal power, and grid and load powers.

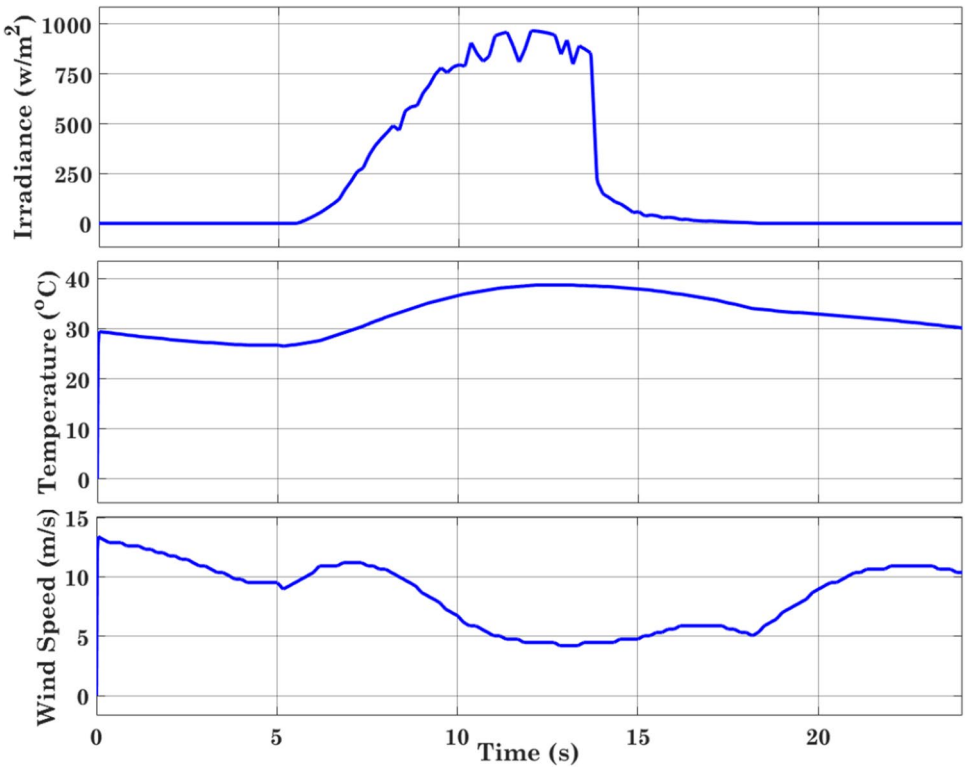

Figure 20. Variation in irradiance, temperature and wind speed.

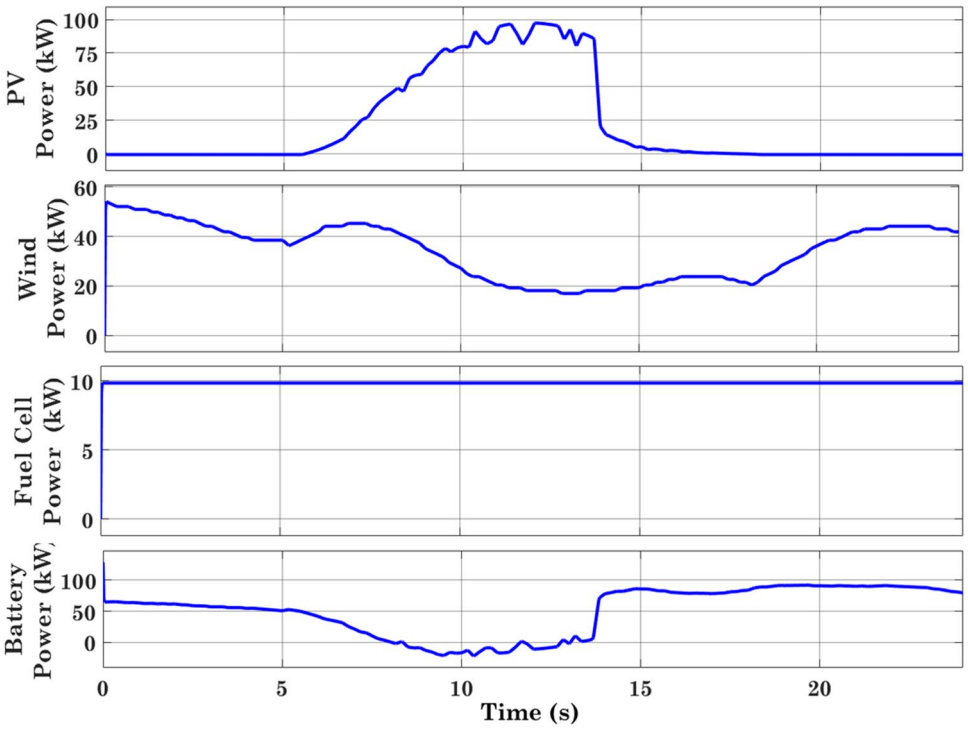

Figure 21. Power created by the PV, wind, fuel and battery cells in kW.

their respective contributions to the microgrid. It includes power data at the battery terminals, showing response of the battery by either charging or discharging based on the available generation and load requirements. The active and reactive powers supplied to both the grid and the load are also shown, offering a holistic view of the power flows within the system and the grid support to the microgrid when needed.

This detailed representation in Fig. 22 emphasizes the complex interactions between the various power sources, the inverter, the battery, and the grid, ensuring that the microgrid operates efficiently and reliably even under fluctuating environmental and load conditions. The ability of the microgrid to adapt to changes in generation and demand is crucial for maintaining power quality and ensuring that the load's energy requirements are consistently met. Figure 23 focuses on the state of charge (SOC) of the battery storage system, presenting its variation over time. The SOC data provide valuable insights into the battery's charging and discharging patterns, which are crucial for understanding the battery in supporting the microgrid during periods of low renewable energy generation or high demand. During periods of excess power generation, the battery enters a charging phase, storing energy for future use. Conversely, during times of insufficient power generation from renewable sources, the battery discharges to provide the necessary power to maintain load balance. This dynamic behavior ensures the reliability of the microgrid, allowing it to meet power demands even when environmental conditions are less favorable.

These results illustrate the operational dynamics and performance metrics of the microgrid system. They demonstrate the system's ability to effectively manage power generation, storage, and distribution under varying environmental conditions, all while maintaining efficient load handling. The combination of optimized PI controllers, renewable energy sources, and battery storage ensures that the microgrid can respond to fluctuations in both generation and demand, providing a reliable and sustainable power supply.

Conclusion

This study presents the development and implementation of a hybrid sine-cosine and spotted Hyena-based chimp optimization algorithm for tuning the PI controllers in a microgrid system. The microgrid comprises photovoltaic (PV) systems, wind energy systems, a fuel cell, and a battery storing system, all of which are related to a common DC bus. The DC bus is interfaced through the main grid through a voltage source converter (VSC). The optimization of eight PI controllers—distributed across the boost converters of the wind, fuel cell, battery energy storage systems, and VSC—ensures efficient energy management and stability of the microgrid. The hybrid SSC algorithm effectively combines the strengths of the sine–cosine algorithm (SCA), spotted

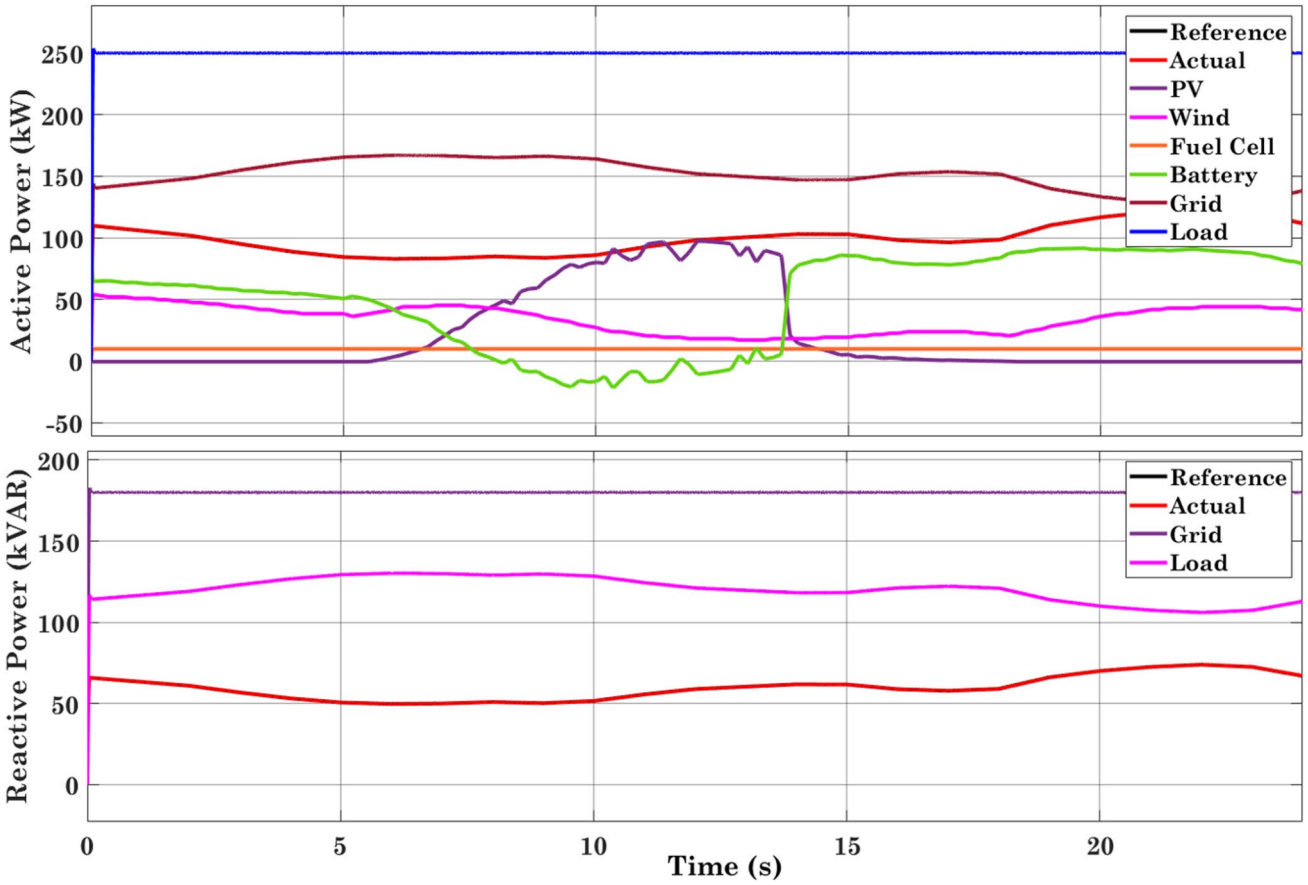

Figure 22. Reference and actual powers of the inverter, PV, wind and fuel cell-generated powers, battery terminal power, and grid and load powers.

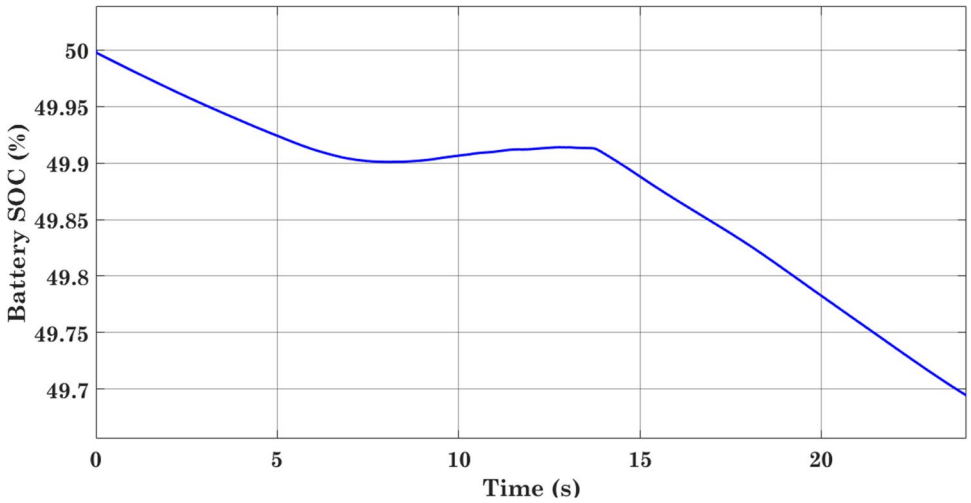

Figure 23. Battery SOC in %.

Hyena optimizer (SHO), and chimp optimization algorithm (ChOA), resulting in improved exploration and exploitation capabilities. The use of the integral of time-weighted squared error (ITSE) as a performance index aided the fine-tuning of the PI controller gains, optimizing the active response and complete performance of the control system. The simulation results, conducted in MATLAB/SIMULINK, demonstrated the execution of the hybrid SSC algorithm compared with traditional optimization methods. The optimized PI controllers showed enhanced stability, reduced overshoot, and faster settling times under varying load and generation conditions. This optimization not only improved the microgrid's operational efficiency but also contributed to the sequence of RES, ensuring a reliable and sustainable power supply. The proposed hybrid SSC process offers a robust and efficient solution for tuning PI controllers in microgrid systems with diverse renewable energy sources. The findings highlight the potential of advanced hybrid optimization techniques in addressing complex control challenges in modern power systems. Future work may focus on real-time implementation and further validation of the algorithm in practical microgrid scenarios.

Data availability

The data that support the findings of this study are available from the corresponding author upon reasonable request.

Received: 9 August 2024; Accepted: 16 October 2024
Published online: 29 October 2024

References

1. Caballero-Pena, J., Parrado-Duque, C. C. Z. A. & German Osma-Pinto. Distributed energy resources on distribution networks: a systematic review of modeling, simulation, metrics, and impacts. *Int. J. Electr. Power Energy Syst.* **138**, 107900 (2022).
2. Raya-Armenta, J. et al. Guerrero. Energy management system optimization in islanded microgrids: an overview and future trends. *Renew. Sustain. Energy Rev.* **149**, 111327 (2021).
3. Mazidi, M., Rezaei, N., Ardakani, F. J., Mohiti, M. & Guerrero, J. M. A hierarchical energy management system for islanded multi microgrid clusters considering frequency security constraints. *Int. J. Elec. Power Energy Syst.* **121**, 106134 (2020).
4. Panda, S., Mohanty, S., Rout, P. K. & Sahu, B. K. Shubhranshu Mohan Parida, Hossam Kotb, Aymen Flah, Marcos Tostado-Véliz, Bdereddin Abdul Samad, and Mokhtar Shouran. An insight into the integration of distributed energy resources and energy storage systems with smart distribution networks using demand-side management. *Appl. Sci.* **12** (17), 8914 (2022).
5. Jin, X., Shen, Y. & Zhou, Q. A systematic review of robust control strategies in DC microgrids. *Electricity J.* **35** (5), 107125 (2022).
6. Zellouma, D., Bekakra, Y. & Benbouhenni, H. Field-oriented control based on parallel proportional–integral controllers of induction motor drive. *Energy Rep.* **9**, 4846–4860 (2023).
7. Fioriti, D., Lutzemberger, G., Poli, D., Duenas-Martinez, P. & Andrea Micangeli. Coupling economic multi objective optimization and multiple design options: a business-oriented approach to size an off-grid hybrid microgrid. *Int. J. Electr. Power Energy Syst.* **127**, 106686 (2021).
8. An, R., Liu, Z., Liu, J. & Liu, B. A comprehensive solution to decentralized coordinative control of distributed generations in islanded microgrid based on dual-frequency-droop. *IEEE Trans. Power Electron.* **37** (3), 3583–3598 (2021).
9. Nour, M. & Magdy, G. José Pablo Chaves-Ávila, Álvaro Sánchez-Miralles, and Francisco Jurado. A new two-stage controller design for frequency regulation of low-inertia power system with virtual synchronous generator. *J. Energy Storage*. **62**, 106952 (2023).
10. Qais, M. H., Hany, M., Hasanien, & Alghuwainem, S. Optimal transient search algorithm-based PI controllers for enhancing low voltage ride-through ability of grid-linked PMSG-based wind turbine. *Electronics*. **9** (11), 1807 (2020).
11. Banakhr, F. A. & Mosaad, M. I. High performance adaptive maximum power point tracking technique for off-grid photovoltaic systems. *Sci. Rep.* **11** (1), 20400 (2021).
12. Wang, Y. et al. A comprehensive review of battery modeling and state estimation approaches for advanced battery management systems. *Renew. Sustain. Energy Rev.* **131**, 110015 (2020).
13. Jiang, Z., Cai, J. & Paul, S. Moses. Smoothing control of solar photovoltaic generation using building thermal loads. *Appl. Energy*. **277**, 115523 (2020).

14. Ioris, D., de Godoy, P. T. & Felisberto, K. D. R. Patrícia Poloni, Adriano Batista De Almeida, and Diogo Marujo. Microgrid Operation and Control: from Grid-connected to Islanded Mode. In *Planning and Operation of Active Distribution Networks: Technical, Social and Environmental Aspects*. 233–256 (Cham: Springer International Publishing, 2022).
15. Yenealem, Mezigebu Getinet, Livingstone MH Ngoo, Dereje Shiferaw, and Peterson Hinga. Management of voltage profile and power loss minimization in a grid-connected microgrid system using fuzzy-based STATCOM controller. *J. Elect. Comput. Eng.* **2020** (1), 2040139 (2020).
16. Benali, A., Khiat, M. & Denai, M. Voltage profile and power quality improvement in photovoltaic farms integrated medium voltage grid using dynamic voltage restorer. *Int. J. Power Electron. Drive Syst. (IJPEDS)*. **11** (3), 481–1490 (2020).
17. Yang, B. et al. Robust fractional-order PID control of supercapacitor energy storage systems for distribution network applications: a perturbation compensation based approach. *J. Clean. Prod.* **279**, 123362 (2021).
18. Quoc, D. V. et al. Tuning PID Controller Bases on Random Search Algorithms. *Int. J. Eng. Res. Technol.* **10** (01), 73–77 (2021).
19. Sztajmec, E. & Szcześniak, P. A review on AC voltage variation compensators in low voltage distribution network. *Energies*. **16** (17), 6293 (2023).
20. George, T. & Ganesan, V. Optimal tuning of PID controller in time delay system: a review on various optimization techniques. *Chem. Prod. Process Model.* **17** (1), 1–28 (2022).
21. Gad, A. G. Particle swarm optimization algorithm and its applications: a systematic review. *Arch. Comput. Methods Eng.* **29** (5), 2531–2561 (2022).
22. Tao, H. et al. Hybridized artificial intelligence models with nature-inspired algorithms for river flow modeling: a comprehensive review, assessment, and possible future research directions. *Eng. Appl. Artif. Intell.* **129**, 107559 (2024).
23. Guo, X., Ji, M., Zhao, Z., Wen, D. & Zhang, W. Global path planning and multiobjective path control for unmanned surface vehicle based on modified particle swarm optimization (PSO) algorithm. *Ocean Eng.* **216**, 107693 (2020).
24. Freitas, D., Lopes, L. G. & Morgado-Dias, F. Particle swarm optimization: a historical review up to the current developments. *Entropy*. **22** (3), 362 (2020).
25. Elhammoudy, A. et al. Dandelion Optimizer algorithm-based method for accurate photovoltaic model parameter identification. *Energy Convers. Management: X.* **19**, 100405 (2023).
26. Dehghani, M., Montazeri, Z., Trojovská, E. & Trojovský, P. Coati optimization algorithm: a new bio-inspired metaheuristic algorithm for solving optimization problems. *Knowl. Based Syst.* **259**, 110011 (2023).
27. Jia, H., Rao, H., Wen, C. & Mirjalili, S. Crayfish optimization algorithm. *Artif. Intell. Rev.* **56** (Suppl 2), 1919–1979 (2023).
28. Alhussan, A. A. et al. A binary waterwheel plant optimization algorithm for feature selection. *IEEE Access.* **11**, 94227–94251 (2023).
29. Heidari, A. A. et al. Harris hawks optimization: Algorithm and applications. *Future Generation Comput. Syst.* **97**, 849–872 (2019).
30. Jia, L. Y., Wang, T., Gad, A. G. & Salem, A. A weighted-sum chaotic sparrow search algorithm for interdisciplinary feature selection and data classification. *Sci. Rep.* **13** (1), 14061 (2023).
31. Manoharan, P. et al. An effective strategy for unit commitment of microgrid power systems integrated with renewable energy sources including effects of battery degradation and uncertainties. *Environ. Sci. Pollut. Res.* **31** (7), 11037–11080 (2024).
32. Wang, M. & Lu, G. A modified sine cosine algorithm for solving optimization problems. *Ieee Access.* **9**, 27434–27450 (2021).
33. Braik, M., Al-Zoubi, H., Ryalat, M., Sheta, A. & Alzubi, O. Memory based hybrid crow search algorithm for solving numerical and constrained global optimization problems. *Artif. Intell. Rev.* **56** (1), 27–99 (2023).
34. Polnik, W., Stobiecki, J., Byrski, A. & Kisiel-Dorohinicki, M. Ant colony optimization–evolutionary hybrid optimization with translation of problem representation. *Comput. Intell.* **37** (2), 891–923 (2021).
35. Xi, L. et al. Chaotic oppositional sine–cosine method for solving global optimization problems. *Eng. Comput.* **38** (2), 1223–1239 (2022).
36. Garg, V. et al. LX-BBSCA: laplacian biogeography-based sine cosine algorithm for structural engineering design optimization. *AIMS Math.* **8** (12), 30610–30638 (2023).
37. Bokam, J. K., Patnana, N., Varshney, T. & Singh, V. P. Sine cosine algorithm assisted FOPID controller design for interval systems using reduced-order modeling ensuring stability. *Algorithms*. **13** (12), 317 (2020).
38. Deng, H., Liu, L., Fang, J., Qu, B. & Huang, Q. A novel improved whale optimization algorithm for optimization problems with multistrategy and hybrid algorithm. *Math. Comput. Simul.* **205**, 794–817 (2023).
39. Pham, V. H. S., Nguyendang, N. T. & Nguyen, N. V. Enhancing engineering optimization using hybrid sine cosine algorithm with Roulette wheel selection and opposition-based learning. *Sci. Rep.* **14** (1), 694 (2024).
40. Dhiman, G. SSC: a hybrid nature-inspired meta-heuristic optimization algorithm for engineering applications. *Knowl. Based Syst.* **222**, 106926 (2021).
41. Liu, W., Moayedi, H., Nguyen, H., Lyu, Z. & Bui, D. T. Proposing two new metaheuristic algorithms of ALO-MLP and SHO-MLP in predicting bearing capacity of circular footing located on horizontal multilayer soil. *Eng. Comput.* **37**, 1537–1547 (2021).
42. Mzili, T., Mzili, I., Riffi, M. E. & Dhiman, G. Hybrid genetic and spotted hyena optimizer for flow shop scheduling problem. *Algorithms*. **16** (6), 265 (2023).
43. Mohammad, S. & Jeebaseelan, S. D. Power flow control of the grid-integrated hybrid DG system using an ARFMF optimization. *Int. J. Electr. Comput. Eng. Syst.* **14** (8), 945–958 (2023).
44. Li, S. et al. A novel rolling optimization strategy considering grid-connected power fluctuations smoothing for renewable energy microgrids. *Appl. Energy*. **309**, 118441 (2022).
45. Hur, S. H. Modelling and control of a wind turbine and farm. *Energy*. **156**, 360–370 (2018).
46. Eltamaly, A. M., Alolah, A. I., Farh, H. M. & Arman, H. Maximum power extraction from utility-interfaced wind turbines. *New Developments Renew Energy*. **8** (1), 159–192 (2013).
47. Diantoro, M. et al. Shockley's equation fit analyses for solar cell parameters from I-V curves. *Int. J. Photoenergy*. **2018** (1), 9214820 (2018).
48. Yang, B. et al. Comprehensive overview of maximum power point tracking algorithms of PV systems under partial shading condition. *J. Clean. Prod.* **268**, 121983 (2020).
49. Sun, D. et al. State of charge estimation for lithium-ion battery based on an Intelligent Adaptive Extended Kalman Filter with improved noise estimator. *Energy*. **214**, 119025 (2021).
50. Dhiman, G. & Kumar, V. Spotted hyena optimizer: a novel bio-inspired based metaheuristic technique for engineering applications. *Adv. Eng. Softw.* **114**, 48–70 (2017).
51. Alabi, T. M. et al. Adeoye, and Bhushan Gopaluni. A review on the integrated optimization techniques and machine learning approaches for modeling, prediction, and decision making on integrated energy systems. *Renew. Energy*. **194**, 822–849 (2022).
52. Khishe, M. & Mosavi, M. R. Chimp optimization algorithm. *Expert Syst. Appl.* **149**, 113338 (2020).
53. NSRDB. (n.d.). https://nsrdb.nrel.gov/.

Author contributions

S.M. carried out the Conceptualization, Methodology, Writing - Original Draft, Data Curation, Formal Analysis, Simulation, Interpretation of results, S.J. carried out the Supervision, Project Administration, Manuscript review and editing.

Funding
This research did not receive any specific grant from funding agencies in the public, commercial, or not-for-profit sectors.

Declarations

Competing interests
The authors declare no competing interests.

Additional information
Correspondence and requests for materials should be addressed to S.M.

Reprints and permissions information is available at www.nature.com/reprints.

Publisher's note Springer Nature remains neutral with regard to jurisdictional claims in published maps and institutional affiliations.

Open Access This article is licensed under a Creative Commons Attribution-NonCommercial-NoDerivatives 4.0 International License, which permits any non-commercial use, sharing, distribution and reproduction in any medium or format, as long as you give appropriate credit to the original author(s) and the source, provide a link to the Creative Commons licence, and indicate if you modified the licensed material. You do not have permission under this licence to share adapted material derived from this article or parts of it. The images or other third party material in this article are included in the article's Creative Commons licence, unless indicated otherwise in a credit line to the material. If material is not included in the article's Creative Commons licence and your intended use is not permitted by statutory regulation or exceeds the permitted use, you will need to obtain permission directly from the copyright holder. To view a copy of this licence, visit http://creativecommons.org/licenses/by-nc-nd/4.0/.

© The Author(s) 2024